# Physics-grounded carrier-phase-space compact model for two-dimensional transistors: Unifying all-region electrical turning points

Hongfu Li,[1,2] Sulin Wang,[3] Léopold Van Brandt,[4] Meihui Zhou,[1] Long Chen,[1] Benjamin Iñiguez,[5] Jean-Pierre Raskin,[4] Denis Flandre,[4] Yuan Liu,[1] Wei-Qing Huang,[1] Lei Liao,[2] and Guoli Li[2,*]

[1] *School of Physics and Electronics, Hunan University, Changsha 410082, China*
[2] *College of Semiconductors (College of Integrated Circuits), Hunan University, Changsha 410082, China*
[3] *School of Mathematics, Hunan University, Changsha 410082, China*
[4] *ICTEAM Institute, Université catholique de Louvain, (UCLouvain), Louvain-la-Neuve 1348, Belgium*
[5] *Department of Electronic Engineering, Universitat Rovira i Virgili, Tarragona 43007, Spain*

(Received 4 July 2025; revised 18 February 2026; accepted 4 May 2026; published 4 June 2026)

Compact models for two-dimensional field-effect transistors (2D FETs), predominantly adapted from conventional unipolar Si metal-oxide-semiconductor FET (MOSFET) frameworks, frequently fail to capture essential physics such as ambipolar conduction, threshold voltage roll-off, and output current upswing in saturation. While models based on Landauer formalism and the Pao-Sah approach offer partial solutions, their reliance on curve fitting and neglect of defects obscure the link to underlying device physics. Here, we introduce a physics-grounded carrier-phase-space (CPS) framework for 2D FET compact modeling. By employing the quasiequilibrium approximation and formulating the drain-source current as a path integral within the CPS, our model accurately describes threshold voltage roll-off, saturation current upswing, and ambipolar behavior. Crucially, analytical expressions for key electrical turning points across all operating regimes, including threshold voltage, saturation voltage, pinch-off voltage, and *p*-*n*-junction onset voltage, are derived for the first time through analysis of the bias-dependent integration path in CPS. Furthermore, the model incorporates the effects of ionized defects and is rigorously validated against experimental data from both ambipolar and unipolar FETs, demonstrating excellent electrostatic gating control and uniform thermal dissipation. This work establishes a comprehensive physics-based CPS compact model for 2D FETs, significantly advancing the foundation for their practical circuit design and manufacturing.

DOI: 10.1103/dmv5-hsxt

## I. INTRODUCTION

CMOS block is the basis for integrated circuits, which require both *n*- and *p*-type transistors [1,2]. In two-dimensional (2D) device technology, the majority carrier type in semiconductors can be dynamically tuned between electrons and holes through electrostatic gating, enabling the reconfigurable operation modes in 2D transistors [1,3]. Such an ambipolar conduction property has been observed in many two-dimensional (2D) diselenides like $WS_2$ [4], $WSe_2$ [5], and $MoS_2$ [6], and is promising for applications in modern circuit design [7–9]. However, a critical challenge in the development of this device technology is compact models, which act as a crucial bridge between semiconductor manufacture and circuit design by translating the device-level physical parameters into circuit-level performance metrics.

A comparison of performance metrics among existing compact models for two-dimensional field-effect transistors (FETs) is summarized in Table I. Previous studies predominantly adapted from conventional unipolar metal-oxide-semiconductor FET (MOSFET) models to analyze the device characteristics of 2D transistors [10]. However, this approach fails to reproduce physical phenomena inherent to 2D FETs, such as ambipolar conduction properties, threshold voltage roll-off, and output current upswing in the saturation region [6,22,23], while also leading to the distortion of parameters like carrier mobility [24,25]. Compact modeling of 2D FETs based on the Landauer formalism primarily focuses on carrier transport across the Schottky barrier [11–15]. Although these models replicate threshold voltage roll-off [12] and ambipolar transport behavior [11,13–15], they are unable to account for the degradation of subthreshold swing caused by the charging and discharging of dynamic defects. From a complementary perspective, Pao-Sah models describe carrier transport through the channel by formulating the current

*Contact author: liguoli_lily@hnu.edu.cn

 

TABLE I. Compact models of 2D FET and performance metrics.

| Performance metrics | MOSFET compact model (EKV) | Landauer 2D FET compact model | Pao-Sah 2D FET compact model | This work |
|---|---|---|---|---|
| Unipolar electrical behavior | **V** [10] | **V** [11–15] | **V** [16–21] | **V** |
| Ambipolar electrical behavior | **X** | **V** [11,13–15] | **V** [16–21] | **V** |
| Threshold voltage roll-off | **X** | **V** [12] | **V** [16,17,20,21] | **V** |
| Subthreshold swing degeneration | **V** [10] | **X** | **V** [16] | **V** |
| Output current upswing in saturation | **X** | **X** | **V** [20] | **V** |
| Physically numerical fitting | **X** [10] | **X** [11,13–15] | **X** [16–19,21] | **V** |
| Analytical solutions for electrical critical points | **V** [10] | **X** | **X** | **V** |

as a path integral in phase space [16–21]. Such models partially address the limitations of Landauer-based models, as they can handle practical subthreshold swing degradation by incorporating terms for ionized defects into the gate electrostatics equations [16]. Nevertheless, these models often introduce numerous parameters with unclear physical meanings [16,19], overlooking requirements for a reduced number of model parameters. Of note, both categories of models overemphasize numerical fitting results while neglecting the connection between the key turning points in device electrical characteristics and their underlying physical mechanisms. They fail to establish an analytical and quantitative link between the phase-transition switching mechanism of 2D semiconductor FETs [26,27] and the experimentally observed threshold voltage roll-off. From a circuit design standpoint, these models cannot assist in predicting the key turning points in device electrical characteristics under a given bias based on material properties (contact barrier height, defect energy-level positions and defect density in the material, and external biases) prior to device fabrication, hindering the optimization of the trade-off between circuit speed and energy consumption [1,28].

In this work, we present a physics-grounded carrier-phase-space (CPS) framework for 2D FET compact modeling. Section II details the assumptions and model construction procedure, including the boundary condition generation and current generation modules (a path integral within the CPS), Here, the physical rationale for the quasiequilibrium approximation (QEA) is addressed. Sections III A and III B present the modeled electrical characteristics and provides explicit analytical expressions for key turning points in transfer and output curves of the ambipolar 2D FETs, such as threshold voltage, saturation voltage, and $p$-$n$-junction onset voltage. Here, the concept of threshold concentration is introduced to connect metal-insulator-transition with electrical turning points. Section III C describes a general method to account for the effect of defects in 2D FETs, herein an additional drift current is computed and the turning points' analytical expressions in device electrical behavior are modified. In Sec. III D, the model is validated by fitting experimental characteristics, for both ambipolar and unipolar transistors. Finally, Sec. IV summarizes the main conclusions of the study.

## II. THEORY AND METHODS

Figure 1(a) illustrates how each module collaborates to derive electrical characteristics for 2D FETs. Based on this schematic, the compact modeling framework mainly consists of boundary condition and current generation modules. Ohmic boundary conditions, determined by external biases ($V_{gs}$, $V_s$, $V_d$), uniquely define the 2D carrier concentrations at the source and drain $n_{2D,s}(V_{gs}, V_s)$, $p_{2D,s}(V_{gs}, V_s)$, $n_{2D,d}(V_{gs}, V_d)$, $p_{2D,d}(V_{gs}, V_d)$. Herein, the boundary-condition equations typically include Gauss law that define the scalar potential of the differential element [DE, in Fig. 1(b)], and statistical mechanics definitions for carriers and ionized defect concentrations. The current generation module produces a specifically defined current $I_{ds} = (W/(y_d - y_s))F(n_{2D,s}, p_{2D,s}, n_{2D,d}, p_{2D,d})$ under given boundary conditions. The intersection of these two modules resides at the scalar potential governed by Gauss law. Therefore, the model construction procedure is as follows: first, specify the scalar potential definition for channel DE; then, establish the boundary-condition equations; finally, formulate the current generation equations.

### A. Boundary-condition generation module

The 2DFET device configuration and its DE definition are depicted in Fig. 1(b). Each DE can be regarded as an infinitely large parallel plate, where the net charge density is the average areal density. Taking the source metal Fermi level as the reference energy $E_{f0}$, the relationship between the DE's net charge density $\sigma_{2D}$ and its scalar potential $\phi_{\text{field}}$ is established by Gauss law:

$$\phi_{\text{field}}(x,y) = V_{gs} + \frac{q}{C'_{\text{eff}}}\sigma_{2D}(x,y) - \frac{E_{f0}}{q} \quad (1)$$

Equation (1) is the gate capacitance electrostatic equation, where $\sigma_{2D}(x,y) = p_{2D}(x,y) - n_{2D}(x,y) + N_D^+(x,y) - N_A^-(x,y)$, $p_{2D}$ and $n_{2D}$ denote the DE's hole and electron

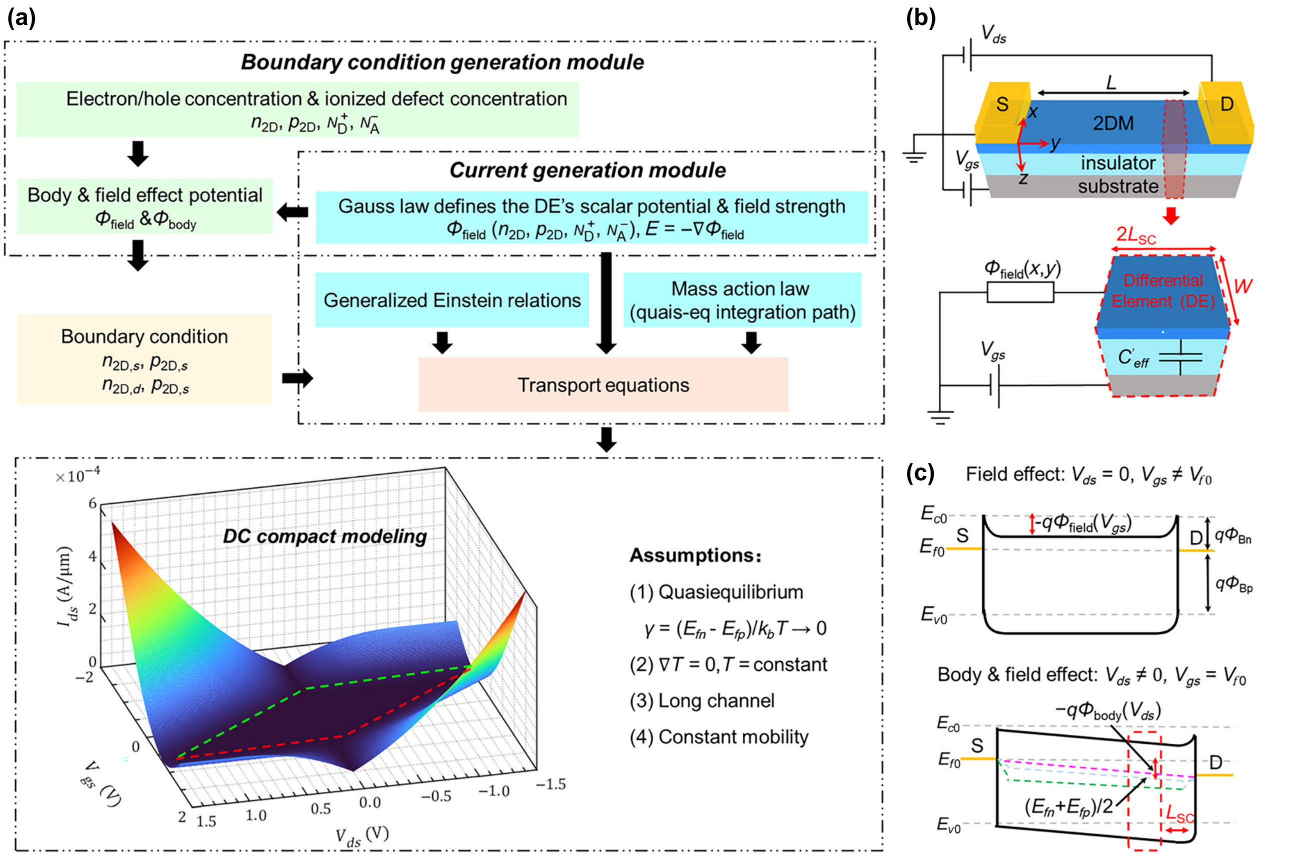


FIG. 1. Compact modeling framework. (a) Boundary condition and current generation modules, illustrating their interaction to determine electrical characteristics of the 2D FETs. Key assumptions are clarified, and the modeled current characteristics are shown. (b) Schematic view of the investigated ambipolar 2D FET and the defined channel differential element. (c) Definitions of the field-effect potential $\Phi_{\text{field}}(x, y)$ and body-effect potential $\Phi_{\text{body}}(x, y)$.

concentration. $N_D^+$ and $N_A^-$ represent the ionized donor and acceptor densities, and $q$ is the positive elementary charge. Given our current focus on a well-performing 2D FET, we neglect contributions of $N_D^+$ and $N_A^-$ and simplify Eq. (1) as $\sigma_{2d} \approx p_{2\text{D}}(x, y) - n_{2\text{D}}(x, y)$. Defect considerations will be addressed in Sec. III C.

The complete boundary-condition generation equations are given by Eqs. (1) and (2) (Sec. 1 of the Supplemental Material [29]). Below, we first define physical meanings of the relevant variables and parameters, then describe detailed derivation of the boundary conditions: $n_{2\text{D},s}$, $p_{2\text{D},s}$, $n_{2\text{D},d}$, and $p_{2\text{D},d}$.

$$n_{2\text{D}} = N_c \ln\left[1 + \exp\left(\frac{\gamma}{2}\right) \exp\left(\frac{\phi_{\text{field}} - \phi_{\text{body}} - \phi_{Bn}}{k_b T/q}\right)\right] \tag{2a}$$

$$p_{2\text{D}} = N_v \ln\left[1 + \exp\left(\frac{\gamma}{2}\right) \exp\left(-\frac{\phi_{\text{field}} - \phi_{\text{body}} + \phi_{Bp}}{k_b T/q}\right)\right] \tag{2b}$$

In Eqs. (1) and (2), $\phi_{Bn(p)}$ represent the electron(hole) Schottky barrier and are defined as $\phi_{Bn} = (E_{c0} - E_{f0})/q > 0$, $\phi_{Bp} = (E_{f0} - E_{v0})/q > 0$. As illustrated in Fig. 1(c), the potentials of $\phi_{\text{field}}(x, y)$ and $\phi_{\text{body}}(x, y)$ are defined as $q\phi_{\text{field}}(x, y) \equiv -(E_c - E_{c0})$, $q\phi_{\text{body}} \equiv -((E_{fn} + E_{fp})/2 - E_{f0})$. The field-effect potential $\phi_{\text{field}}(x, y)$ quantifies band-edge displacement of conduction minimum ($E_c$) relative to the flat-band condition ($E_{c0}$), while the body effect potential $\phi_{\text{body}}(x, y)$ characterizes the movement of the Fermi level [or average of quasi-Fermi level, $(E_{fn} + E_{fp})/2$] relative to the reference energy ($E_{f0}$). Hence, $\phi_{\text{body}}(x, y)$ represents the increment in system's energy (i.e., Fermi level) through charge exchange between source-drain electrodes and the 2D channel. $\phi_{\text{field}}(x, y)$ merely causes the redistribution of charge carriers within the system, without introducing net charge or altering the Fermi level.

The parameter $\gamma$ used in Eqs. (1) and (2) is a dimensionless quantity, which is defined as $\gamma = (E_{fn} - E_{fp})/k_b T \propto \ln(n_{2\text{D}} p_{2\text{D}}/n_i^2)$ and represents the nonequilibrium degree within the DE. For direct band-gap semiconductors, for example the majority of the monolayer 2D semiconductors [30], $\gamma$ is positively correlated with the DE's net recombination rate $R_{\text{direct}}$, where $R_{\text{direct}} =$

$R_{ec}(n_{2D}p_{2D} - n_i^2)$ with $R_{ec}$ and $n_i$ denoting the recombination coefficient and intrinsic carrier concentration, respectively. For a monolayer 2D semiconductor channel, $\gamma > 0$ signifies nonequilibrium carrier injection into the DE, causing recombination to exceed thermal generation. Under this condition, the DE operates as a resistor. Conversely, $\gamma < 0$ indicate carrier extraction from DE, where thermal generation dominates recombination, enabling the DE to function as a power source. In most scenarios, 2D transistors function like resistors, implying $\gamma > 0$ in any DE. According to the energy band diagram of a *p*-*n* junction [31], $|\gamma|$ scales with electric-field strength $E$ (i.e., the scalar potential gradient). This enables estimation of a DE's $|\gamma|$ through the average field strength in channel direction: $|\bar{E}| \approx |V_{ds}/L| \propto |\gamma v_t/L_{sc}|$, where $L_{sc}$ is the 2D semiconductor screen length and $v_t = k_bT/q$ is the thermal voltage.

Given parameters of $\gamma$, $\phi_{\text{body}}$ and temperature ($T$), Eqs. (1) and (2) can generate $n_{2D}$, $p_{2D}$, and $\phi_{\text{field}}$ within any DE. For DEs near the source and drain, it is acceptable to assume that $\phi_{\text{body},d} = V_d$, $\phi_{\text{body},s} = V_s$ (equivalent to Ohmic contact), but determining their $\gamma$ remains challenging. According to Schottky's or Bethe's contact theory [31], it is possible to identify a DE in which the carrier concentration is unaffected by the net current and maintains its equilibrium value. This implies such DE satisfies $\gamma \to 0^+$(i.e., quasiequilibrium), and shall be located at least a $L_{sc}$ away from the contact interface. If the FET channel is sufficiently long, we can always find such a DE to compute the boundary conditions.

### B. Current generation module

In this section, the drift-diffusion transport equations are employed to derive the path integral expression for device current, as the characteristic length ($L_{sc}$) in 2D semiconductor is typically approximately 10 nm [32] and the channel length of our studied 2D transistors significantly exceeds this value. When device size shrinks to the ballistic limit(carrier mean free path ≈ channel length) or quantum transport regime(channel length ≈ carrier de Broglie wavelength), the classical-statistics-based DD model immediately fails [33].

Electric-field strength $E$ is defined as the negative gradient of scalar potential. Combining Eq. (1), we obtain

$$E(y) = -\frac{d\phi_{\text{field}}}{dy} = -\frac{q}{C'_{\text{eff}}}\left(\frac{dp_{2D}}{dy} - \frac{dn_{2D}}{dy}\right) \tag{3}$$

$$\frac{I_e(y)}{W} = -\frac{q^2}{C'_{\text{eff}}}\mu_n n_{2D}\left(\frac{dp_{2D}}{dy} - \frac{dn_{2D}}{dy}\right) + qD_n\frac{dn_{2D}}{dy} \tag{4a}$$

$$\frac{I_h(y)}{W} = -\frac{q^2}{C'_{\text{eff}}}\mu_p p_{2D}\left(\frac{dp_{2D}}{dy} - \frac{dn_{2D}}{dy}\right) - qD_p\frac{dp_{2D}}{dy} \tag{4b}$$

In 2D materials system, quantum confinement along the out-of-plane direction, modifies both the band structure and Einstein's diffusion-mobility ratio (DMR). Unlike bulk semiconductors ($D_{n(p)} = (k_bT/q)\,\mu_{n(p)}$), the ratio in 2D semiconductors can be derived from the generalized Einstein relation [34], while merely considering the primary contribution of the first sub-band carriers (see Sec. 2 of the Supplemental Material [29]):

$$D_n = \frac{k_bT}{q}\mu_n\frac{n_{2D}}{N_c}\frac{\exp(n_{2D}/N_c)}{\exp(n_{2D}/N_c) - 1} \tag{5a}$$

$$D_p = \frac{k_bT}{q}\mu_p\frac{p_{2D}}{N_v}\frac{\exp(p_{2D}/N_v)}{\exp(p_{2D}/N_v) - 1} \tag{5b}$$

Under dc conditions, the current continuity equation dictates that current through any channel DE is constant. Integrating from source ($s$) to drain ($d$) yields the drift and diffusion components of electron and hole currents, which satisfy $I_e = I_{\text{drift},e} + I_{\text{diff},e}$, $I_h = I_{\text{drift},h} + I_{\text{diff},h}$:

$$I_{\text{drift},e} = -\frac{W}{y_d - y_s}\frac{q^2}{C'_{\text{eff}}}\int \mu_n n_{2D}(dp_{2D} - dn_{2D})_\tau, \tag{6a}$$

$$I_{\text{diff},e} = +qN_c\frac{W}{y_d - y_s}\int_{n_{2D,s}}^{n_{2D,d}} D_n d\left(\frac{n_{2D}}{N_c}\right), \tag{6b}$$

$$I_{\text{drift},h} = -\frac{W}{y_d - y_s}\frac{q^2}{C'_{\text{eff}}}\int \mu_p p_{2D}(dp_{2D} - dn_{2D})_\tau, \tag{6c}$$

$$I_{\text{diff},h} = -qN_v\frac{W}{y_d - y_s}\int_{p_{2D,s}}^{p_{2D,d}} D_p d\left(\frac{p_{2D}}{N_v}\right). \tag{6d}$$

As demonstrated by the above equations, the device total current ($I_{ds} = I_e + I_h$) can be formulated as a path integral in CPS (Fig. 2), without an explicit dependence on spatial coordinates. Here, we define $\tau$ as the integration path, represented by a curve in CPS. All points on the curve satisfy Eqs. (1) and (2), and $\tau$ starts at $(n_{2D,s}, p_{2D,s})$ and ends at $(n_{2D,d}, p_{2D,d})$. However, the precise trajectory of $\tau$ is unspecified. Under the finite-element method (FEM), this ambiguity does not arise because mapping points throughout the phase space are determined by simultaneously solving the drift-diffusion (DD), current continuity (CE), thermal conduction (TCE), and Poisson equations (PEs) for all the channel DEs. If we designate the path $\tau$ obtained via FEM as the true integration path $\tau_{tr}$, then the core challenge for compact modeling of 2D FETs is to derive an approximation path that replaces $\tau_{tr}$ while reproducing identical current values. The specific solution can be given by Eq. (7) under $\gamma = 0$, and defined as the quasiequilibrium path $\tau_{qe}$. Justification for this approach is presented below.

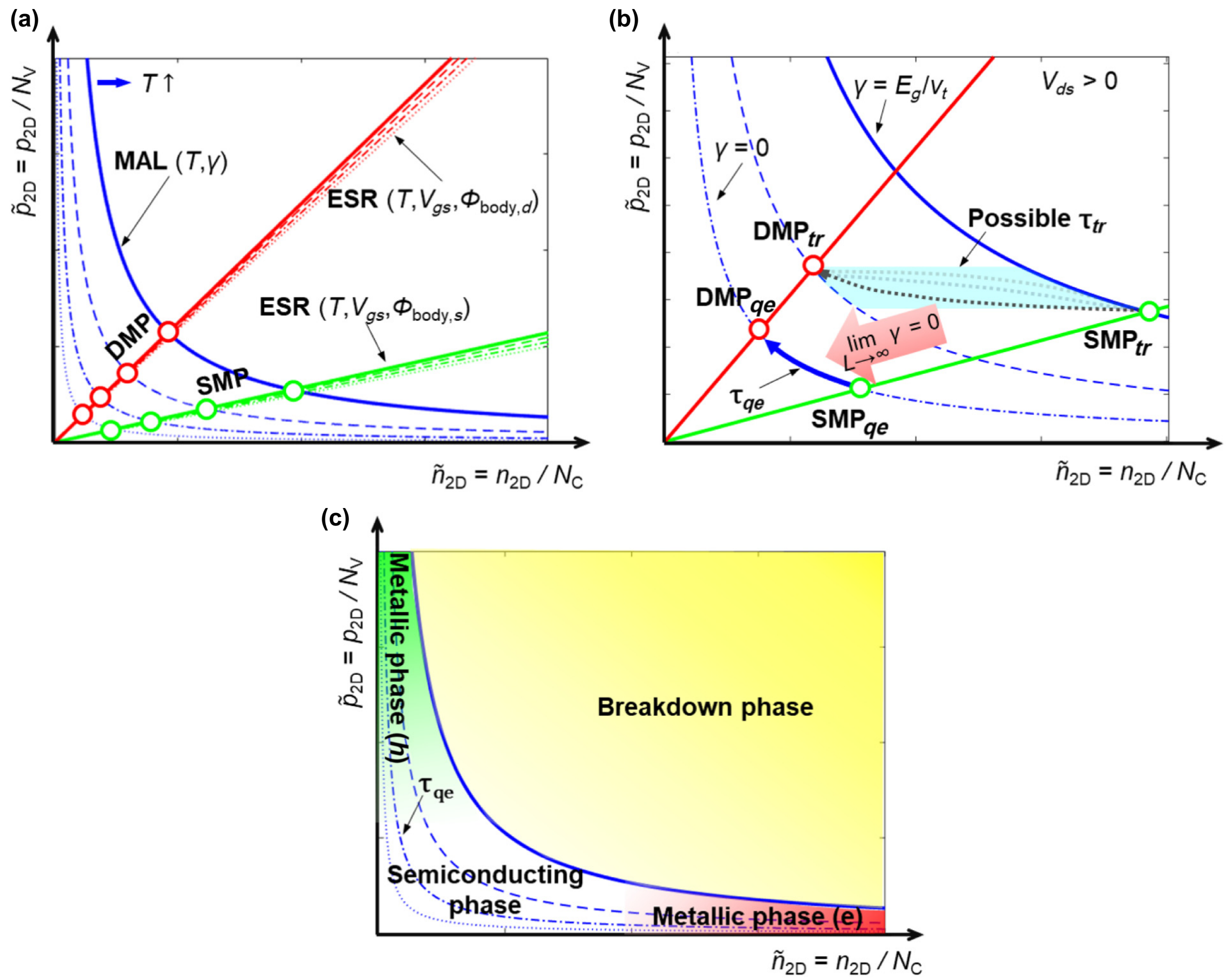


FIG. 2. Carrier phase space and current integration path. (a) Reduced CPS. The blue lines represent the mass action law (MAL) at various temperature $T$ and nonequilibrium degree $\gamma$. Red and green lines represent the electrostatic restriction (ESR) of the drain and source DEs, respectively. Here, the mapping points of the source and drain DEs (SMP and DMP) corresponds to intersections of the MAL and ESR curves, determined by $\gamma$, $\phi_{\text{body},s}$, $\phi_{\text{body},d}$, and $T$. (b) True current integration path $\tau_{tr}$ obtained via the finite-element method, and the quasiequilibrium path $\tau_{qe}$ under the approximation of $\gamma \to 0^+$. At $V_{ds} > 0$, SMP lies to the lower right of DMP in the reduced CPS. (c) Phase division of the 2D semiconductors, showing the semiconducting, metallic, and breakdown phases.

To readily justify the validity of quasiequilibrium path (QEP) approach, we recast Eqs. (1) and (2) as Eqs. (7) and (8). In Fig. 2(a), the blue line represents the mass action law [MAL, Eq. (7)] under various $T$ and $\gamma$, while the red and green lines represent the electrostatic restriction [ESR, Eq. (8)] of the DEs at drain and source, respectively, under a specific set of conditions ($T$, $V_{gs}$, $\phi_{\text{body}}$). Here, we defined the reduced carrier concentration as $\tilde{n}_{2D} = n_{2D}/N_c$, $\tilde{p}_{2D} = p_{2D}/N_v$. The intersection of the MAL [Eq. (7)] and ESR [Eq. (8)] curves corresponds to the DE's mapping point in the reduced CPS. Consequently, the mapping point of the source DE in this reduced CPS is termed as the source mapping point (SMP), the mapping point of the drain DE is similarly defined as the drain mapping point (DMP). The operation of a FET relies on the transport of nonequilibrium majority carriers. Specifically, for $n$-channel conduction and $V_{ds} > 0$, the nonequilibrium electrons are injected from the source contact into the 2D channel. In this case, as dictated by Eqs. (7) and (8), SMP must lie to the lower right of DMP in the reduced CPS, which are correspondingly represented by SMP$_{tr}$ and DMP$_{tr}$ in Fig. 2(b) along the true integration path $\tau_{tr}$. Experiments have demonstrated that 2D FET operates in accumulation mode, and the accumulated carriers originate from electrical injection at the source and drain contacts [6]. Therefore, it is reasonable to assume that the hole/electron concentration reaches its maximum within the DEs near the terminal contacts and decreases monotonically from one terminal to the other. Therefore, $\tau_{tr}$ should reside within the dashed blue region depicted in Fig. 2(b). If the channel is sufficiently long, satisfying $|\gamma| \approx |\bar{E}/(v_t/L_{sc})| \approx |(V_{ds}/v_t)(L_{sc}/L)| \ll E_g/k_bT$

(where $E_g$ is the band gap), then the nonequilibrium majority carrier concentration will be significantly lower than its equilibrium concentration. Consequently, $\gamma \to 0^+$ for any DE inside the 2D channel, implying $\mathrm{SMP}_{tr} \to \mathrm{SMP}_{qe}$, $\mathrm{DMP}_{tr} \to \mathrm{DMP}_{qe}$, and $\tau_{tr}$ approaches $\tau_{qe}$ [see Sec. 10 of Supplemental Material [29] for a comparison in currents obtained from full numerical drift-diffusion simulation ($\tau_{tr}$) and quasiequilibrium approximation modeling ($\tau_{qe}$)].

$$\left[\exp\left(\frac{n_{2D}}{N_c}\right)-1\right]\left[\exp\left(\frac{p_{2D}}{N_v}\right)-1\right]=\exp\left(\frac{\gamma k_b T-E_g}{k_b T}\right) \tag{7}$$

$$\frac{\exp\left(\frac{n_{2D}}{N_c}\right)-1}{\exp\left(\frac{p_{2D}}{N_v}\right)-1}\exp\left[\frac{2\frac{q}{C'_{eff}}(n_{2D}-p_{2D})}{v_t}\right]=\exp\left(\frac{2V_{gs}-2\phi_{body}-2\frac{E_{f0}}{q}+\phi_{Bp}-\phi_{Bn}}{v_t}\right) \tag{8}$$

Strictly speaking, when considering the practical implications of energy dissipation in 2D electronics, DEs along the semiconductor channel operates at different temperatures [35]. This thermal gradient alters the integration path, as designated by the arrow in Fig. 2(a). However, under idealized heat-dissipation conditions, we neglect the self-heating effect and assume uniform temperature operation across the channel DEs. Figure 2(c) depicts the phase divisions for 2D semiconductors, including the semiconducting, metallic and breakdown phases. And the metallic phase is achieved when the DEs are saturated with holes or electrons.

After replacing by the quasi-equilibrium path $\tau_{qe}$, the $I_{ds}$ expression reduces from the general form in Eqs. (6a)–(6d) to the following special case Eq. (9):

$$I_e=+\frac{W}{y_d-y_s}\mu_n\int_{\tilde{n}_{\mathrm{2D},s}}^{\tilde{n}_{\mathrm{2D},d}}\mathrm{integ}_n(\tilde{n}_{\mathrm{2D}})d\tilde{n}_{\mathrm{2D}}, \tag{9a}$$

$$I_h=-\frac{W}{y_d-y_s}\mu_p\int_{\tilde{p}_{\mathrm{2D},s}}^{\tilde{p}_{\mathrm{2D},d}}\mathrm{integ}_p(\tilde{p}_{\mathrm{2D}})d\tilde{p}_{\mathrm{2D}}. \tag{9b}$$

The integrands $\mathrm{integ}_n(\tilde{n}_{\mathrm{2D}})$ and $\mathrm{integ}_p(\tilde{p}_{\mathrm{2D}})$ are nondecreasing functions, with their analytical forms detailed in Sec. 3 of Supplemental Material [29]. More specific drift and diffusion contribution is provided in Sec. 3 of Supplemental Material [29]. By setting $\gamma\ = 0$ and eliminating both the $\phi_{\mathrm{field}}$ and $\tilde{p}_{\mathrm{2D}}$ (or $\tilde{n}_{\mathrm{2D}}$) terms from Eqs. (1) and (2), we obtain Eq. (10). Here $V_{f0}=E_{f0}/q$. Based on Eq. (10), the DE's majority carrier switches from electrons to holes while $V_{gs}$ sweeping from positive to negative infinity, as illustrated in Fig. 3(d). Crucially, Eqs. (10a) and (10b) determine the starting (SMP) and ending (DMP) points of the integration path under a specific bias condition. Moreover, the hole and electron currents ($I_h$, $I_e$) obtained via this QEP approach depends solely on the projection of the integration path onto the hole and electron axes in this reduced CPS, because the integral $\mathrm{integ}_n(\tilde{n}_{\mathrm{2D}})$, $\mathrm{integ}_p(\tilde{p}_{\mathrm{2D}})$ are the functions of $\tilde{n}_{\mathrm{2D}}$ and $\tilde{p}_{\mathrm{2D}}$, respectively. This feature will be utilized to identify the minimum point of transfer curve in the next section.

## III. MODELING AND DISCUSSION

### A. Transfer characteristics

Transfer characteristics of an ideal ambipolar 2D FET are presented in Figs. 3 and 4(a). As shown in Figs. 3(a) and 3(b), the hole threshold voltage ($V_{th,\,p}$) exhibits a positive shift under $V_{ds}$, while the electron threshold voltage ($V_{th,\,n}$) shows a negative shift under negative $V_{ds}$. This phenomenon is commonly called threshold voltage ($V_{th}$) roll-off in transistors [23]. Previous studies typically interpret this behavior as follows:

$$v_t ln\left[\exp(\tilde{n}_{2d})-1\right]-\frac{q}{C'_{eff}}\left[N_V\ln\left(1+\frac{\exp\left(\frac{-E_g}{k_bT}\right)}{\exp(\tilde{n}_{2d})-1}\right)-N_C\tilde{n}_{2d}\right]=V_{gs}-\phi_{body}-V_{f0}-\phi_{Bn} \tag{10a}$$

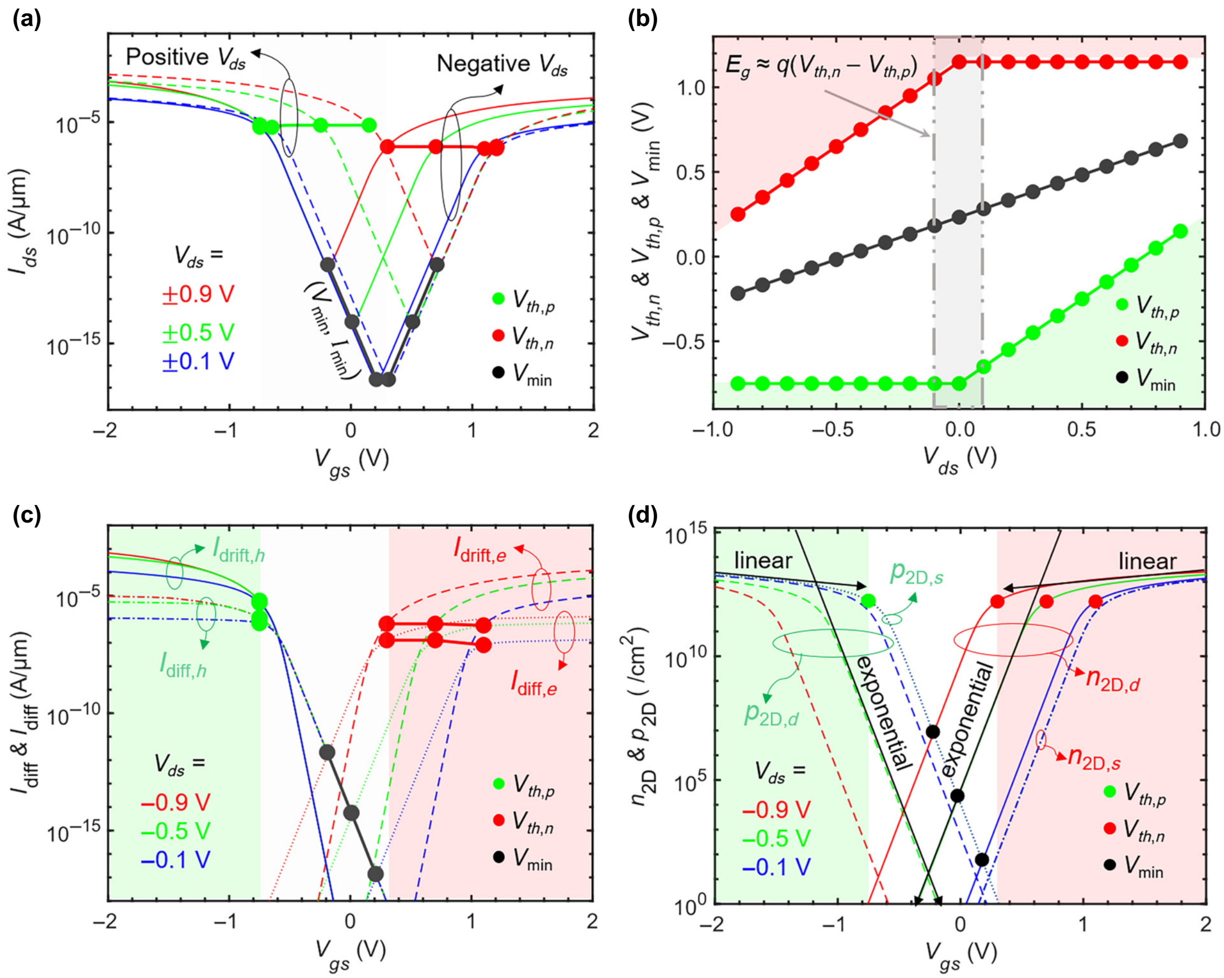


FIG. 3. Transfer characteristics modeling for ambipolar 2D FETs. (a) Device transfer curves ($I_{ds}$ vs $V_{gs}$), under various drain bias $V_{ds}$. (b) Threshold voltages for $n$- and $p$-type operation modes, $V_{th,n}$ and $V_{th,p}$, which are obtained from Eqs. (12a) and (12b). The diamond-shaped boundary dividing the on- and off-state regions are also observed in experiment [36]. (c) Transfer characteristics modeling for ambipolar 2D FETs with demonstration of the relative contribution for drift and diffusion. The diffusion current ($I_{\text{diff},e}$ and $I_{\text{diff},h}$) dominates in the off-state while the drift current ($I_{\text{drift},e}$ and $I_{\text{drift},h}$) dominates in the on-state. (d) Electron and hole concentrations within the source and drain DEs ($n_{2\text{D},s}$, $p_{2\text{D},s}$, $n_{2\text{D},d}$, $p_{2\text{D},d}$) as a function of $V_{gs}$. The black dots represent the lowest-point voltage $V_{\min}$, obtained from Eq. (13).

$$v_t ln\left[\exp\left(\tilde{p}_{2d}\right)-1\right]+\frac{q}{C'_{eff}}\left[N_V\tilde{p}_{2d}-N_C\ln\left(1+\frac{\exp\left(\frac{-E_g}{k_bT}\right)}{\exp\left(\tilde{p}_{2d}\right)-1}\right)\right]=-V_{gs}+\phi_{body}+V_{f0}-\phi_{Bp} \tag{10b}$$

the charge type ($n$ or $p$) in the contact depletion region is governed by electrostatic doping within the channel, which means the Schottky barrier conduction voltages for electrons (or holes) shift under varying bias conditions [12,13,37]. Herein, we aim to analyze carrier transport within the FET channel, clarify the physical mechanisms corresponding to each scenario in the transfer characteristics, and finally elucidate the quantitative relationship between the threshold voltage and specific conditions like biasing voltage, contact properties (e.g., effective Schottky barrier height), and device defects.

### *1. Threshold carrier concentration and voltage*

While employing the QEP approach ($\gamma = 0$), carriers' concentration given by Eqs. (2a) and (2b) are simplified to

$$n_{2\text{D}} = N_c \ln\left[1+\exp\left(\frac{\phi_{\text{field}}-\phi_{\text{body}}-\phi_{Bn}}{v_t}\right)\right], \tag{11a}$$

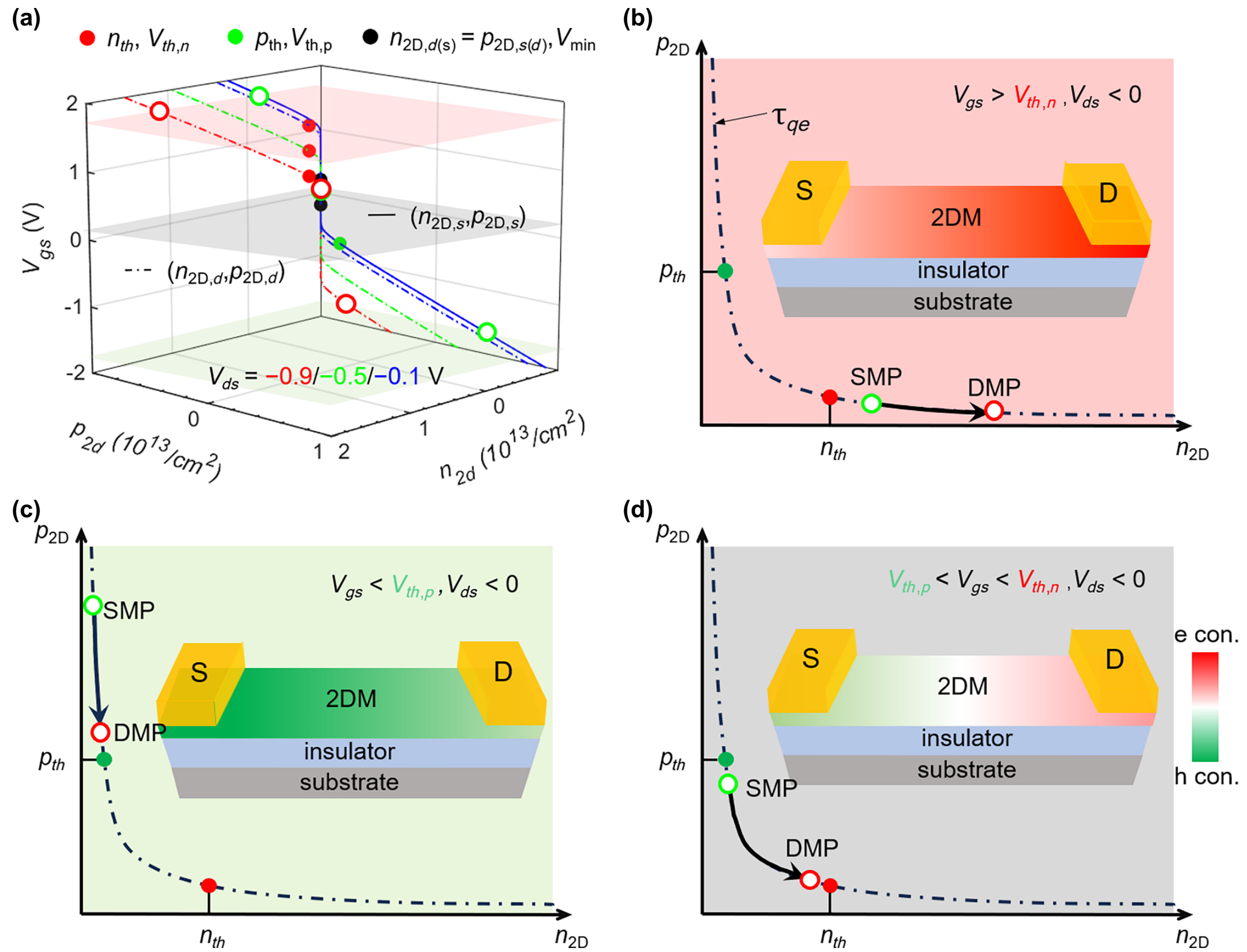


FIG. 4. Current integration path vs $V_{gs}$ in CPS. (a) All DE's response toward the external bias of $V_{gs}$, represented by a family of curves, $(n_{2D}, p_{2D}, V_{gs})$. Projections of the intersection points between the $V_{gs}$ cross section and this family of curves constitute the quasiequilibrium path $\tau_{qe}$ in CPS. (b)–(d) Typical current integration paths for the $n$-type conduction, $p$-type conduction, and off state. The red and green dots represent the threshold carrier concentrations for hole and electron, $n_{th}$ and $p_{th}$, which separately correspond to the threshold voltages of $V_{th,n}$ and $V_{th,p}$. The black dot represents the specific status of $n_{2D,s(d)} = p_{2D,s(d)}$ at the lowest point in transfer curve $V_{\min}$.

$$p_{2D} = N_v \ln\left[1 + \exp\left(\frac{-\phi_{\text{field}} + \phi_{\text{body}} - \phi_{Bp}}{v_t}\right)\right]. \quad (11b)$$

In a 2D FET, the threshold voltage $V_{th}$ is typically defined as the gate voltage $V_{gs}$ at which the Fermi level $E_f$ aligns with the conduction- or valence-band edge ($E_c$ or $E_v$) of the semiconductor channel. However, in practical devices, the local $V_{th}$ for each discrete DE varies spatially along the channel. The measured $V_{th}$ represents a macroscopic turning point, reflecting the equivalent manifestation of all channel elements as an entirety. Therefore, it is necessary to clarify phase transition of the individual DEs before assessing collective electrical behavior of the 2D transistor.

According to Eqs. (11a) and (11b), the dependence of $n_{2D}$ on $V_{gs}$ transitions from exponential to linear when $E_c$ drops below $E_f$. Similarly, the $p_{2D}(V_{gs})$ relationship transitions from exponential to linear when $E_v$ rises above $E_f$, as shown in Fig. 3(d). Thus, the designated DE undergoes a transition between the semiconducting and metallic phases, which corresponds to dielectric response change. Under the metallic phase, the DE's net charge density follows $Q'_{\text{net}} = C'_{\text{eff}}(V_{gs} - V_{th}) \approx q(p_{2D} - n_{2D})$, $C'_{\text{eff}}$ is the effective capacitance per unit area. Under the semiconducting phase, $Q'_{\text{net}}(V_{gs})$ follows an exponential trend. Herein, the turning points in the $n_{2D}(V_{gs})$ and $p_{2D}(V_{gs})$ curves demarcate the boundary between semiconducting and metallic phases. And these critical carrier concentrations are designated as the electron (hole) threshold concentration $n_{th}(p_{th})$ for these 2D transistors. By setting the left-hand term of Eqs. (10a) and (10b) to zero, $n_{th}$ and $p_{th}$ for the designated DE can be obtained at a given $\phi_{\text{body}}$, which are irrelated to the applied bias and exclusively determined by $C'_{\text{eff}}$, electron (hole) density of states $N_c(N_v)$, and temperature $T$. This parametric independence suggests that threshold concentration should be a more accurate indicator of device characteristics than threshold voltage. Setting the right-hand side of Eqs. (10a) and (10b) to zero, the DE's threshold voltage $V_{th,n}(V_{th,p})$ corresponding to $n_{th}(p_{th})$ are obtained. For the case of ideal Ohmic contact, $\phi_{\text{body},s} = V_s$ and $\phi_{\text{body},d} = V_d$, threshold voltage in the ambipolar transistors without ionized defect effects can be expressed below:

$$V_{th,n(p)} = \phi_{\text{body},d(s)} \pm \phi_{Bn(p)} + V_{f0},\quad -\frac{E_g}{q} < \phi_{\text{body},d} - \phi_{\text{body},s} < 0, \tag{12a}$$

$$V_{th,n(p)} = \phi_{\text{body},s(d)} \pm \phi_{Bn(p)} + V_{f0},\quad 0 < \phi_{\text{body},d} - \phi_{\text{body},s} < \frac{E_g}{q}. \tag{12b}$$

When $V_{ds} < 0$, it is evident that $V_{th,n}$ depends on the drain DE and $V_{th,p}$ depends on the source DE. Here, holes dominate as the majority carriers in the channel DEs, flowing from source to drain. The hole injection terminates effectively when the source DE transitions out of its (hole-filled) metallic phase, triggering the entire channel transition to the semiconducting phase (off state). Consequently, by increasing $V_{gs}$ within this regime, the channel transitions out of the semiconducting phase only when the drain DE enters its (electron-filled) metallic phase. On the other aspect, when $V_{ds} > 0$, an analogous analysis can be carried out following the same methodology. Based on the foregoing discussion and the modeled results in Fig. 3, our proposed Pao-Sah class model, built upon the CPS framework, effectively unifies the ambipolar electrical behavior in 2D FETs and maintains compatible physical picture with the Landauer-based compact model for A2DFETs [11–15].

As represented by red and green dots in Figs. 3(a) and 3(c), the threshold voltages $V_{th,n}$ and $V_{th,p}$ defined in Eqs. (12a) and (12b) correspond to the gate-voltage value where the drift current $I_{\text{drift}}$ inside the channel exceeds the diffusion current $I_{\text{diff}}$. This definition is consistent with the conventional understanding of the MOSFET's threshold voltage, where $I_{\text{drift}}$ dominates in the on state and $I_{\text{diff}}$ becomes dominant in the off state. Furthermore, our model shows that the diffusion current remains constant throughout the on-state operation of the A2DFETs. Notably, a diamond-shaped boundary dividing the on-state and off-state regions is depicted in Figs. 1(a) and 3(b). This phenomenon has also been observed in previously reported experiments on 2D FETs [36]. Our modeling attributes this to the fact that, when establishing the boundary conditions [Eqs. (12a) and (12b)] for the 2D transistors, the primary contribution from the first sub-band was considered. According to Eqs. (12a) and (12b), the diamond-shaped boundary of the $I_{ds}(V_{gs}, V_{ds})$ surface is sensitive to the SBH. Experiments confirmed that the threshold voltage of the device shifts when only the contact electrode is replaced [38], which means this boundary shape distorts or shifts significantly if the contact barriers were asymmetric or negligible. Furthermore, if the impact of the second sub-band cannot be neglected, a second diamond-shaped boundary would be expected to appear. $V_{n,th}$ and $V_{p,th}$ are plotted in Fig. 3(b).

It should be noted that the band-gap values were directly deduced from $V_{th,n} - V_{th,p} \approx E_g/q$, based on electrical characterizations of the 2D transistors with the aggressively scaled gate dielectrics (e.g., ionic liquid gating) [5]. However, this electrical extraction technique is only suitable under conditions of low defect density and $|V_{ds}|$, because the $V_{th}$ extraction necessitates linear extrapolation of the transfer curve's off-state region in a logarithmic scale. For devices with substantial bulk or interface defects, subthreshold swing degradation would result in significant discrepancies and systematic deviation between the electrically extracted $E_g$ and that obtained through optical characterization [5].

### *2. Current integration path in carrier phase space*

According to Eqs. (10a) and (10b), the DE's response to an external bias of $V_{gs}$ can be represented by a family of curves, $F(n_{2D}, p_{2D}, V_{gs}, \phi_{\text{body}}(y)) = 0$, which are plotted in Fig. 4(a). Here, the projections of the intersection points between the $V_{gs}$ cross section and this family of curves constitute the quasiequilibrium path $\tau_{qe}$ in CPS. Under specific conditions, namely on state ($V_{gs} > V_{th,n}$ for $n$-type, $V_{gs} < V_{th,p}$ for $p$-type) and off state ($V_{th,p} < V_{gs} < V_{th,n}$) of the ambipolar 2D FETs, the corresponding current integral paths are depicted in Figs. 4(b)–4(d), respectively. As demonstrated in Sec. II B, while employing the QEP approach, the current components of $I_e$ and $I_h$ exclusively depend on the $\tau_{qe}$ projection onto the electron and hole axes. Herein, a specific operation point must exist where the sum of the projected lengths is minimized, leading to the lowest device current in the transfer curves, i.e., $(V_{\min}, I_{\min})$. For an A2DFET satisfying $\mu_n/\mu_p \in [0.1, 10]$, an approximate solution is to configure SMP and DMP symmetrically about the line $n_{2D} = p_{2D}$ in the phase space, namely $n_{2D,s(d)} = p_{2D,d(s)}$. For an ideal A2DFET, $V_{\min}$ always occurs at (see Sec. S4 of the Supplemental Material [29]):

$$V_{\min} = \frac{\phi_{\text{body},s} + \phi_{\text{body},d}}{2} + V_{f0} - \frac{\phi_{Bp} - \phi_{Bn}}{2}. \tag{13}$$

Obviously, $V_{\min}$ is associated with the electron and hole barriers $\phi_{Bn}$, $\phi_{Bp}$ at the metal-semiconductor contacts. When $\phi_{Bp} \approx 0$ and $\phi_{Bn} \approx E_g$, $V_{\min} > 0$; conversely, when $\phi_{Bp} \approx E_g$ and $\phi_{Bn} \approx 0$, $V_{\min} < 0$. Numerical verification of Eq. (13) is displayed as the black dots in Figs. 3(a)–3(d) and 4(a).

### B. Output characteristics

The output characteristics obtained from $\tau_{qe}$ are shown in Figs. 5 and 6(a). Next, we will clarify physical mechanisms underlying each scenario of output curves and provide analytical expressions for the key turning points when A2DFETs operate in linear, saturation and $p$-$n$-junction onset regimes.

#### *1. Saturation and p-n-junction onset voltages*

Based on the modeled transfer characteristics and experimental observations, it is evident that the electrical characteristics of A2DFETs fundamentally reflect the phase transition of the 2D channel between semiconducting and metallic phases under an external electric field [26,27,39]. For a sufficiently long channel, the state of the source DE is confined by the combined influence of gate and source fields, which determines the magnitude and polarity (electron or hole) of the output saturation current. As a result, carriers' concentrations of the source DE, $n_{2D,s}$, and $p_{2D,s}$, as shown in Figs. 5(d) and 6(a), remain invariant to $V_{ds}$. When $V_{gs} > V_{th,n}$ and $V_{ds} = 0$, the entire 2D channel is situated in the electron-filled metallic phase. By increasing $V_{ds}$, electrons are progressively extracted from the channel, and the drain DE transitions from the initial metallic phase, through the semiconducting phase, and eventually reaches the hole-filled metallic phase. This phase transition corresponds to the linear region, saturation region, and $p$-$n$-junction onset region in output characteristics of the A2DFETs, as shown in Figs. 5(a) and 6(a). As illustrated in Figs. 5(a) and 5(c), the electron current $I_e$ dominates the channel while the 2D FET operates in the linear and saturation regimes. In contrast, an additional hole current $I_h$ arise in the $p$-$n$-junction onset region. At $V_{ds} > 0$, $I_e$ flows from

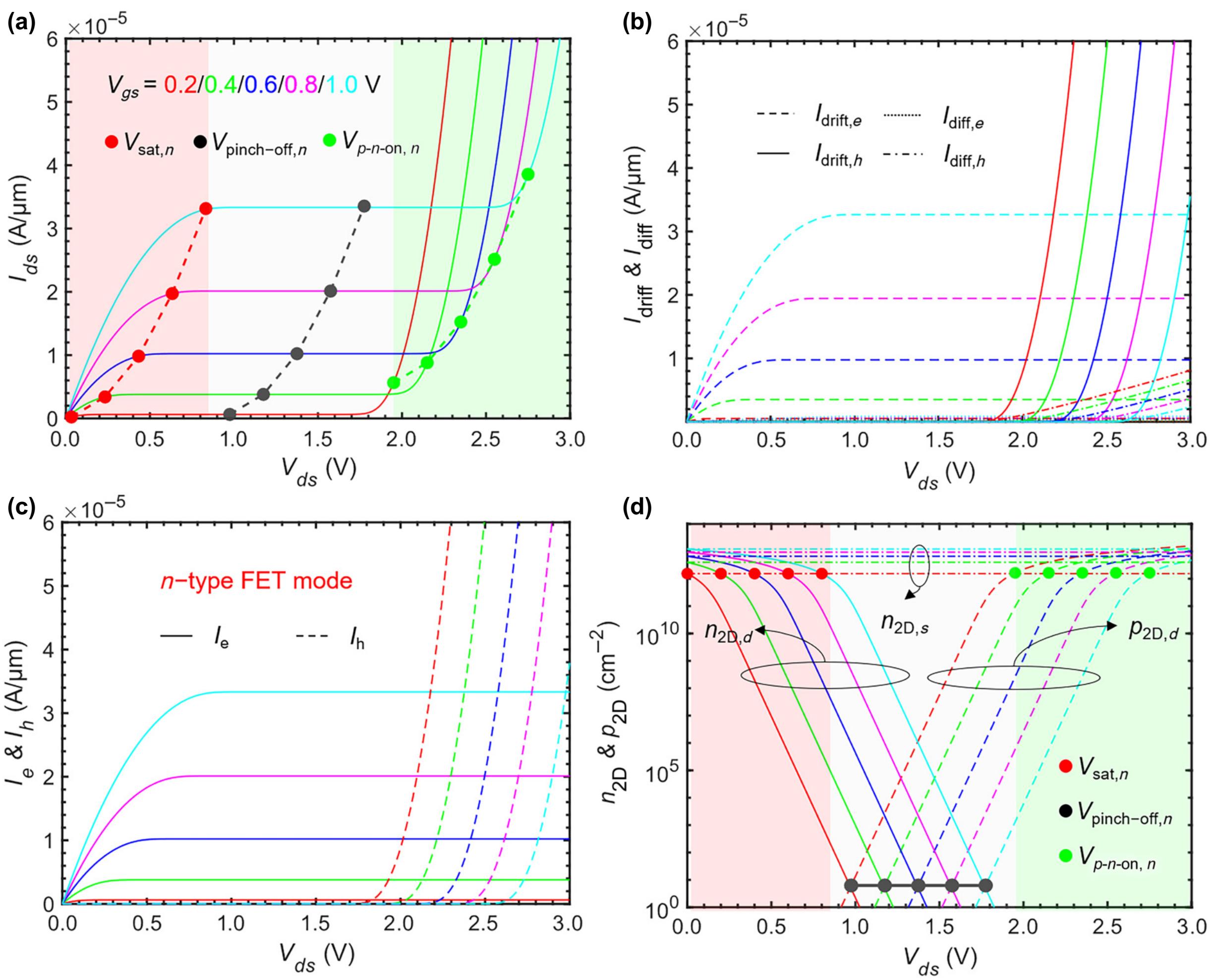


FIG. 5. Output characteristics modeling for ambipolar 2D FETs. (a) Device output curves ($I_{ds}$ vs $V_{ds}$), specifically for $n$-type conduction. (b) Diffusion and drift currents components for electrons and holes. (c) Electron and hole currents as a function of $V_{ds}$. In the $n$-type conduction, electron current $I_e$ dominates in the saturation region. Hole current $I_h$ dominates in the $p$-$n$-junction onset region. (d) Electron and hole concentrations within the source and drain DEs ($n_{2D,s}$, $p_{2D,s}$, $n_{2D,d}$, $p_{2D,d}$). The red and green dots represent the saturation voltage $V_{sat}$ and $p$-$n$-junction onset voltage $V_{p\text{-}n\text{-on}}$, as validated by Eqs. (14a) and (14b). The black dots represent the pinch-off voltage $V_{\text{pinch-off}}$ in Eq. (15).

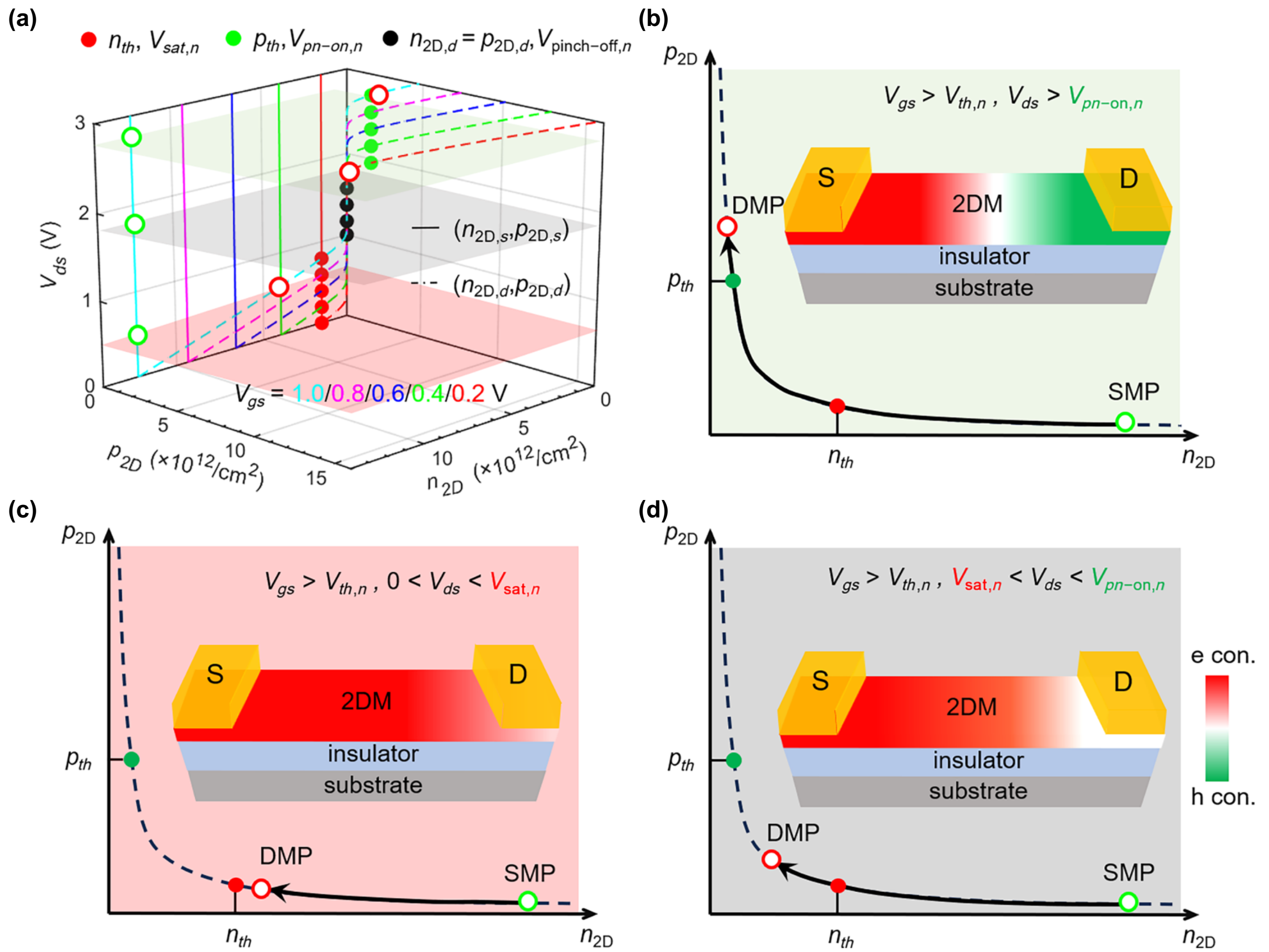

FIG. 6. Current integration path vs $V_{ds}$ in CPS. (a) Carriers' concentrations at the source and drain DEs as a function $V_{ds}$. For the long channel, $n_{2D,s}$ and $p_{2D,s}$ keeps constant, whereas $n_{2D,d}$ and $p_{2D,d}$ changes with $V_{ds}$. (b)–(d) Current integration paths under the linear region, the saturation region and the $p$-$n$-junction onset region. The red and green dots represent $n_{th}$ and $p_{th}$, which separately correspond to the saturation voltage $V_{\mathrm{sat},n}$ and $p$-$n$-junction onset voltage $V_{p\text{-}n\text{-on},n}$. The black dot represents pinch-off, here $p_{2D,d} = n_{2D,d}$.

drain to source, indicating that the source serves as an electron reservoir and the drain acts as a hole reservoir. Since carrier injection from the source is constrained by gate and source biases, hole injection from the drain increases with $V_{ds}$; as a result, the current increment observed in the $p$-$n$-junction onset region (at high $V_{ds}$) is mainly attributed to the holes. This regime also degrades the subthreshold slope of the 2D FETs under large $|V_{ds}|$ [13].

Therefore, applying the same methodology used to derive $V_{th,n(p)}$, the saturation voltage $V_{\mathrm{sat}}$ and $p$-$n$-junction onset voltage $V_{p\text{-}n\text{-on}}$ observed in the $n$- and $p$-type ideal A2DFET output curves are analytically expressed below:

$$V_{\mathrm{sat},n(p)} = V_{gs} \mp \phi_{Bn(p)} - V_{f0}, \tag{14a}$$

$$V_{p\text{-}n\text{-on},\,n(p)} = V_{gs} \pm \phi_{Bp(n)} - V_{f0}. \tag{14b}$$

Verification of $V_{\mathrm{sat}}$ and $V_{p\text{-}n\text{-on}}$ are represented as the red and green dots in Figs. 5(a), 5(d), and 6(a).

### 2. Pinch-off and switching capability degradation

Carriers' concentrations at the source and drain DEs are plotted in Fig. 6(a) as a function of $V_{ds}$. Representatively considering the $n$-type conduction ($V_{gs} > V_{th,n}$), the phase-space diagrams corresponding to the linear ($0 < V_{ds} < V_{\mathrm{sat},n}$), saturation ($V_{\mathrm{sat},n} < V_{ds} < V_{p\text{-}n\text{-on},n}$), and $p$-$n$-junction onset regions ($V_{ds} > V_{p\text{-}n\text{-on},n}$) of the A2DFET are shown in Figs. 6(b)–6(d). Following the conventional definitions about MOSFET, the pinch-off voltage $V_{\text{pinch-off}}$ is identified as the $V_{ds}$ value when the net charges density at the drain DE vanishes ($\sigma_{2D,d} = 0$). Under the defect-free conditions, this implies $p_{2D,d} = n_{2D,d}$. Herein, $V_{\text{pinch-off}}$ for 2DFETs is derived as follows (see Sec. S4 of the Supplemental Material [29]):

$$V_{\text{pinch-off}} = V_{gs} - V_{f0} + \frac{\phi_{Bp} - \phi_{Bn}}{2}. \tag{15}$$

As validated by the black points in Figs. 5(a), 5(d), and 6(a), pinch-off in 2D FETs does not signify the output saturation, but indicates the phase transition of the drain DE from metallic to semiconducting. In these devices, pinch-off occurs in middle of the saturation and satisfies the relation: $V_{\text{pinch-off}} = (V_{\text{sat},n} + V_{p\text{-}n\text{-on},p})/2$. However, constrained by the conventional MOSFET theory, a prevalent misconception is that output saturation in 2D FETs was primarily attributed to pinch-off or self-heating [40].

Therefore, based on the current integral paths derived from the output modeling [Figs. 6(b)–6(d)], two critical issues can be addressed for these 2D FETs: (i) the validity of Eqs. (12a) and (12b) at $|V_{ds}| < E_g/q$; (ii) the degradation of switching capability under high $|V_{ds}|$. First, to ensure effective turn-off capability, it is essential to maintain the device channel in its semiconductor state. As shown in Fig. 4(d), under moderate $V_{ds}$, there exists a specific $V_{gs}$ range where the projection of the 2D channel in CPS is entirely confined within the semiconducting phase; in contrast, under high $|V_{ds}|$, the situation depicted in Fig. 6(b) will inevitably occur. Specifically, regardless of the $V_{gs}$ adjustments, certain regions close to source or drain contacts persistently remain in the metallic phase, thereby degrading the turn-off capability. Consequently, the 2D FET operates like a forward-biased $p$-$n$ junction, exhibiting sustainable conduction even in the nominally off state [6,13]. Under such conditions, Eqs. (12a) and (12b) become invalid, and abnormally $V_{th,n} < V_{th,p}$. If the A2DFET channel comprises a single-layer direct-band-gap semiconductor (e.g., $MoSe_2$, $WS_2$, $WSe_2$ [3]), direct recombination predominates in carriers' recombination process. Thus, a light-emission region can be observed within the 2D channel, spatially corresponding to the $p$-$n$-junction depletion zone [41,42]. This electroluminescent state has been harnessed to realize the light-emitting transistors in experiments [41,43].

### C. Defect consideration

To account for the defect charging and discharging effects in the 2D FETs, an additional drift current $I_{\text{trap}}$ arising from the ionized defect field must be discussed, given by $I_{\text{trap}} = (W/(y_d - y_s))F(N^-_{A,s}, N^+_{D,s}, N^-_{A,d}, N^+_{D,d})$, and the expressions for $V_{th}$, $V_{\text{sat}}$, and $V_{p\text{-}n\text{-on}}$ require modification.

$$\begin{aligned} N_D^+ &= \frac{N_d}{1+g_d\exp(E_{fn}-E_d/k_bT)} = \frac{N_d}{1+(g_d/[\exp(p_{2\text{D}}/N_v)-1])\exp((\phi_{\text{don}}-(E_g/q))/v_t)} \\ &= \frac{N_d}{1+g_d[\exp(n_{2\text{D}}/N_c)-1]\exp(\phi_{\text{don}}/v_t)} \end{aligned} \tag{16a}$$

$$\begin{aligned} N_A^- &= \frac{N_a}{1+g_a\exp(E_a-E_{fp}/k_bT)} = \frac{N_a}{1+(g_a/[\exp(n_{2\text{D}}/N_c)-1])\exp((\phi_{\text{acc}}-(E_g/q))/v_t)} \\ &= \frac{N_a}{1+g_a[\exp(p_{2\text{D}}/N_v)-1]\exp(\phi_{\text{acc}}/v_t)} \end{aligned} \tag{16b}$$

$$\begin{aligned} N_D^+ &= \sum_{i=1}^{n}\frac{N_{d,i}}{1+g_d\exp\left(\frac{E_{fn}-E_{d,i}}{k_bT}\right)} = N_{d,\text{tot}}\left\{1-\frac{\ln[1+(\exp(E_g/k_bT)/g_d)(\exp(p_{2\text{D}}/N_v)-1)]}{(\exp(E_g/k_bT)/g_d)\left(\exp\left(\frac{p_{2\text{D}}}{N_v}\right)-1\right)}\right\} \\ &= N_{d,\text{tot}}\left\{1-\frac{\ln[1+(1/g_d(\exp(n_{2\text{D}}/N_c)-1))]}{1/g_d(\exp(n_{2\text{D}}/N_c)-1)}\right\} \end{aligned} \tag{17a}$$

$$\begin{aligned} N_A^- &= \sum_{j=1}^{m}\frac{N_{a,j}}{1+g_a\exp[(E_{a,j}-E_{fp})/k_bT]} = N_{a,\text{tot}}\left\{1-\frac{\ln[1+(\exp(E_g/k_bT)/g_a)(\exp(n_{2\text{D}}/N_c)-1)]}{(\exp(E_g/k_bT)/g_a)(\exp(n_{2\text{D}}/N_c)-1)}\right\} \\ &= N_{a,\text{tot}}\left\{1-\frac{\ln[1+(1/g_a(\exp(p_{2\text{D}}/N_v)-1))]}{1/g_a(\exp(p_{2\text{D}}/N_v)-1)}\right\} \end{aligned} \tag{17b}$$

#### 1. *Defects modeling under QEA*

As shown in Fig. 7(a), the donor and acceptor levels are specified: $\phi_{\text{don}} = (E_c - E_d)/q$, $\phi_{\text{acc}} = (E_a - E_v)/q$. The ionized defects' density is determined by the convolution integral between the distribution function of defect states density and the Fermi-Dirac distribution of holes and electrons within the band-gap region. Here, the expressions of $N_A^-(n_{2\text{D}}, p_{2\text{D}})$ and $N_D^+(n_{2\text{D}}, p_{2\text{D}})$ vary with the

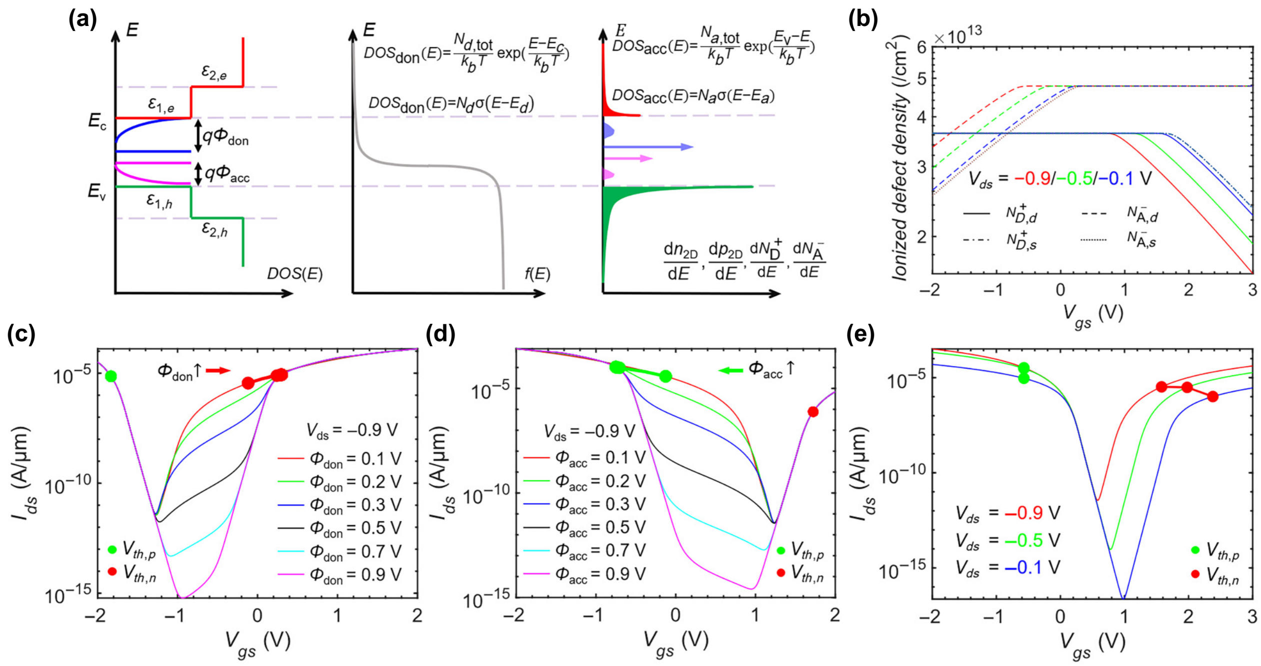


FIG. 7. Defect effects on device characteristics. (a) Defect distribution profiles within 2D semiconductors. The left panel depicts the density of states (DOS) of acceptor and donor located within the 2D band gap. Here, $\varepsilon_{1,e(h)}$ and $\varepsilon_{2,e(h)}$ represent the first and second subbands of the conduction (valence) band [44]. The purple and pink curves represent exponential decay band-tail donors and acceptors, respectively. Conversely, the straight lines indicate single energy-level donor and acceptor. The middle panel shows the Fermi-Dirac distribution function. The right panel illustrates that the ionized defects density is calculated by convolving the Fermi-Dirac function with the bandgap DOS. (b) Ionized donor and acceptor densities ($N_D^+$ and $N_A^+$) as a function of $V_{gs}$, specifically described by Eqs. (17a) and (17b) for exponentially decaying band-tail defect (EDBTD). (c) and (d) Effect of a single-energy level donor and acceptor on device transfer curves, under different trap-energy levels. The red and green dots are verified by Eqs. (20a) and (20b). (e) Effect of the exponential decaying band-tail defect on transfer characteristics.

defect distribution function. Next, the single-energy-level defect (SELD) and exponentially decaying band-tail defect (EDBTD) are representatively examined.

For SELD, the ionized donor and acceptor concentration ($N_D^+$ and $N_A^-$) can be described by Eq. (16) (see Sec. S5 of the Supplemental Material [29]). Here $g_d$ and $g_a$ represent the degeneracy of donors and acceptors, respectively. $N_d$ and $N_a$ denote the corresponding defect states density, respectively.

For EDBTD, $N_D^+$ and $N_A^-$ can be rewritten as Eq. (17a) (see Sec. S5 of the Supplemental Material [29]). Here $N_{d,\mathrm{tot}}$ and $N_{a,\mathrm{tot}}$ denote the total density of state for the tail-distributed donors and acceptors, respectively.

Now, considering the influence of ionized donors and acceptors, $N_D^+$ and $N_A^-$, Eq. (1) can be transformed into

$$\phi_{\mathrm{field}} = V_{gs} + \frac{q}{C'_{\mathrm{eff}}}(p_{2\mathrm{D}} - n_{2\mathrm{D}} + N_D^+ - N_A^-) - \frac{E_{f0}}{q}. \quad (18)$$

Here, the DE's electrical response to external fields critically depends on the $N_D^+$ and $N_A^-$ functions. Therefore, to achieve the optimal agreement between compact modeling and experimental characterization, it is imperative to appropriately select the defect distribution profiles for these 2D FETs. The additional current components attributed to the ionized defect are expressed as follows:

$$I_{\mathrm{trap}} = I_{\mathrm{trap},e} + I_{\mathrm{trap},h}, \quad (19a)$$

$$I_{\mathrm{trap},h} = -\frac{W}{L}\frac{q^2}{C'_{\mathrm{eff}}}\mu_n \int_{n_{2\mathrm{D},s}}^{n_{2\mathrm{D},d}} n_{2\mathrm{D}}\{dN_D^+(n_{2\mathrm{D}}) - dN_A^-(n_{2\mathrm{D}})\}, \quad (19b)$$

$$I_{\mathrm{trap},h} = -\frac{W}{L}\frac{q^2}{C'_{\mathrm{eff}}}\mu_p \int_{p_{2\mathrm{D},s}}^{p_{2\mathrm{D},d}} p_{2\mathrm{D}}\{dN_D^+(p_{2\mathrm{D}}) - dN_A^-(p_{2\mathrm{D}})\}. \quad (19c)$$

Consequently, the additional drift current arising from SELD and EDBTD are derived in detail in Sec. S5 of the Supplemental Material [29]. For the SELD case, the device drain currents are presented in Figs. 7(c) and 7(d) in which the discrete acceptor and donor are separately considered. Figure 7(e) shows the modeled transfer curves under the EDBTD condition, correspondingly $N_D^+$ and $N_A^-$ at the source and drain DEs are plotted in Fig. 7(b) as a function of $V_{gs}$.

### 2. Effect on $V_{th}$, $V_{sat}$, and $V_{p\text{-}n\text{-}on}$

The preceding framework defines threshold voltages $V_{th,n}$ and $V_{th,p}$ as the gate bias where the Fermi level aligns with the 2D band edges. At this point, carrier concentrations reach the threshold value. Accounting for the ionized defect effects, the $V_{th}$ expressions are modified as Eqs. (20a) and (20b). Here, $V_{th,n}$ and $V_{th,p}$ depend on the defects distribution within the bandgap. For discrete deep-level defects, $\phi_{\text{don}}$ and $\phi_{\text{acc}}$ exceed $5\upsilon_t$, the proposed formulas demonstrate their excellent accuracy. However, the substantial shallow-level defects induce band-gap narrowing effect. As a result, to maintain the precise estimation of threshold voltage and optimal fitting of device electrical characteristics, appropriate adjustment of band-gap parameters is essential. Numerical verification of Eqs. (20a) and (20b) is denoted by the red and green points in Figs. 7(c) and 7(d). Similarly, the analytical formulas for the saturation voltage $V_{\text{sat}}$ and $p$-$n$-junction onset voltage $V_{p\text{-}n\text{-}\text{on}}$ are revised in Sec. S6 of the Supplemental Material [29].

$$V_{th,n(p)} = \phi_{body,d(s)} \pm \phi_{Bn(p)} + V_{f0} - \frac{q}{C'_{eff}}\{N_D^+[\tilde{n}_{th}(\tilde{p}_{th})] - N_A^-[\tilde{n}_{th}(\tilde{p}_{th})]\}, \quad -\frac{E_g}{q} < \phi_{body,d} - \phi_{body,s} < 0 \tag{20a}$$

$$V_{th,n(p)} = \phi_{body,s(d)} \pm \phi_{Bn(p)} + V_{f0} - \frac{q}{C'_{eff}}\{N_D^+[\tilde{n}_{th}(\tilde{p}_{th})] - N_A^-[\tilde{n}_{th}(\tilde{p}_{th})]\}, \quad 0 < \phi_{body,d} - \phi_{body,s} < \frac{E_g}{q} \tag{20b}$$

According to Eqs. (20a) and (20b), the threshold voltage in a 2D FET can be precisely engineered through the following approaches: (i) metal-semiconductor interface engineering (including top and edge contacts) to achieve effective control of the Schottky barrier heights ($\phi_{Bn}$ and $\phi_{Bp}$); (ii) gate capacitance design (via dielectric material selection and thickness optimization) enabling precise manipulation of the threshold carrier concentration ($n_{th}$ and $p_{th}$); (iii) defect engineering, involving manipulation of the defect energy level and density. It is also worth pointing

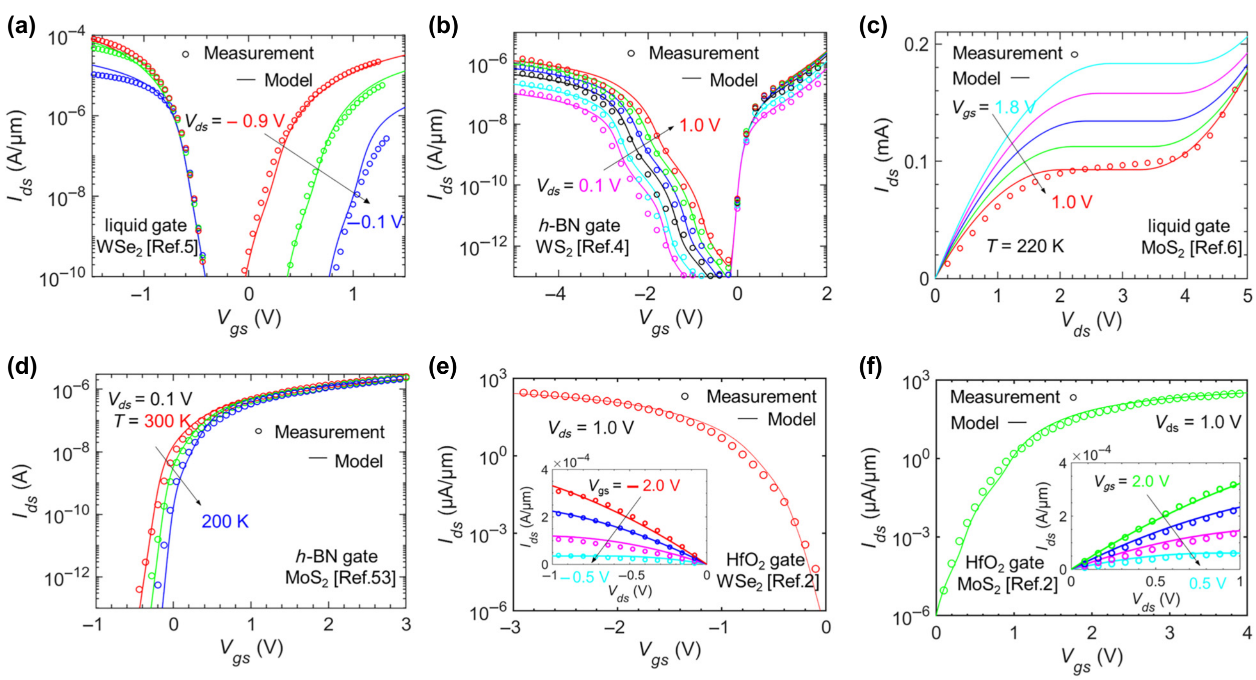


FIG. 8. Verification between experimental measurement and model characteristics. (a),(b) Transfer curves ($I_{ds}$ vs $V_{gs}$) for ionic liquid gated $WSe_2$ FET and $h$-BN gated $WS_2$ FET. (c) Output curves ($I_{ds}$ vs $V_{ds}$) for liquid-gated $MoS_2$ ambipolar transistor at 220 K. (d) The transfer curve fitting results for the same $MoS_2$ FETs under different temperature with the same parameters. At lower temperature ranges, the transport mechanism switches from band transport to hopping, which therefore falls outside the applicable scope of our work [45]. (e),(f) The fitting results for the unipolar 2D FET. Compact modeling fitting parameters are listed in Tables II and III.

TABLE II. Intrinsic device parameters.

| Figure | Channel material | $V_{f0}$ (V) | $T$ (K) | $\phi_{Bn}$ (V) | $\phi_{Bp}$ (V) | $\mu_n$ (cm$^2$/Vs) | $\mu_p$ (cm$^2$/Vs) | $L$ (μm) | $W$ (μm) | EOT (nm) |
|---|---|---|---|---|---|---|---|---|---|---|
| 8(a) | $WSe_2$ (2L) [5] | 0.0 | 340 | 1.10 | 0.45 | 15.5 | 75.0 | 2 | 1.5 | 0.7 |
| 8(b) | $WS_2$ (bulk) [4] | 0.0 | 300 | 0.15 | 1.20 | 214 | 3.0 | 2 | 10 | 11.10 |
| 8(c) | $MoS_2$ (bulk) [6] | −1.8 | 220 | 0.55 | 0.85 | 13.7 | 17.0 | 7 | 10.8 | 1.45 |
| 8(d) | $MoS_2$(1L) [53] | 0.0 | … | 0.4 | 1.3 | 25 | 0.0 | 6.2 | 4.0 | 6.5 |
| 8(e) | $WSe_2$ (2L) [2] | 0.0/1.5 | 330 | 0.01 | 1.50 | 0.0 | 12.8 | 0.1 | 0.5 | 2.0 |
| 8(f) | $MoS_2$ (1L) [2] | 0.0/-1.3 | 350 | 1.0 | 0.9 | 11.3 | 0.0 | 0.1 | 0.5 | 2.0 |
| 3&4(a) | $WSe_2$ (2L) [5] | 0.0 | 380 | 1.15 | 0.75 | 10.5 | 80 | 2 | 1.5 | 0.7 |
| 5&6(a) | $WSe_2$ (2L) [5] | −0.9 | 380 | 1.10 | 0.85 | 21 | 80 | 2 | 1.5 | 0.7 |

**Note:** The electron and hole relative effective mass ($m_e^*$ and $m_h^*$) are intrinsic material parameters and merely defined by band structure properties of the 2D semiconductors [51,52]. For $WSe_2$, $m_e^*/m_h^* = 0.35/0.41$; for $WS_2$, $m_e^*/m_h^* = 0.37/0.45$; for $MoS_2$, $m_e^*/m_h^* = 0.59/0.44$. And the electron and hole valley degeneracy ($g_{v,e}$ and $g_{v,h}$) and the electron and hole spin degeneracy ($g_{s,e}$, and $g_{s,h}$) are intrinsic material parameters and physically determined by the band structure of the 2D semiconducting channel. For transition metal dichalcogenides, they are typically taken as $g_{v,e(h)} = 4$ and $g_{s,e(h)} = 2$, respectively [51,52]. In Figs. 8(e) and 8(f), transfer curve fitting set $V_{f0} = 0$, but output curves fitting set $V_{f0} = 1.5$ and $V_{f0} = -1.3$ for $p$-channel and $n$-channel, respectively. Because the $I_{ds}$ measurement date in Ref. [2] plot against gate overdrive voltage.

out, shallow-level defects (below $5v_t$) minimally impact the subthreshold swing of the 2D FETs, but causes a parallel shift in transfer characteristics and degrades the on-off current ratio, because of the band-gap narrowing effect. In contrast, deep-level defects significantly degrade the subthreshold characteristics and facilitate expansion of the off-state region in Figs. 7(c)–7(e).

### D. Experimental validation

Figure 8 verifies our compact model by comparing the theoretical (lines) and experimental (symbols) results for both transfer (i.e., $I_{ds}$ vs $V_{gs}$) and output (i.e., $I_{ds}$ vs $V_{ds}$) characteristics. The experimental data were obtained from two distinct device configurations: the ionic liquid gated and hexagonal boron nitride ($h$-BN) gated ambipolar FETs [4–6]. In these configurations, the ionic liquid gate acts as an efficient cooling system, resulting in low-temperature gradients ($\nabla T$) in the semiconductor channel. Furthermore, the stacked $h$-BN structure exhibits excellent heat dissipation, because of enhanced phonon transmission at the lattice-matched between 2D and $h$-BN interface [46]. These carefully engineered configurations validate our fundamental assumption of excellent heat-dissipation capabilities in 2D FETs, specifically $\nabla T = 0$ throughout the entire channel. Here, the Schottky barrier heights are suggested to be extracted by Arrhenius plot [47]. Noting that, the reverse saturation current corresponding to the top-contact and edge-contact configurations has different temperature dependencies in 2D FETs [48]. Hall measurements are recommended for determining electron and hole mobilities ($\mu_n$ and $\mu_p$), instead of the conventional extraction methods (e.g., MOSFET mobility [47]) that are based on unipolar MOSFET compact model. Although precise characterization of defect energy levels is generally unavailable in experiments, photoluminescence spectroscopy can be utilized to extract specific information regarding the donor and acceptor energy levels, distribution and density profiles [49]. However, for multilayered two-dimensional semiconductors with an indirect band gap, more sophisticated experimental methods are required to obtain information on their defect energy levels and densities [50] (see Sec. S9 of the Supplementary Material [29] for a specification of the parameter physical meanings and defect-related parameter extraction). Effective mass ($m_e^*$, $m_h^*$), valley degeneracy ($g_{v,e}$, $g_{v,h}$), and spin degeneracy ($g_{s,e}$, $g_{s,h}$) of the 2D materials are referred to in

TABLE III. Defect fitting parameters.

| Figure | Channel material | $\phi_{\text{don},1}$ (V) | $N_{d,1}$ (/cm$^2$) | $\phi_{\text{don},2}$ (V) | $N_{d,2}$ (/cm$^2$) | $\phi_{\text{acc},1}$ (V) | $N_{a,1}$ (/cm$^2$) | $\phi_{\text{acc},2}$ (V) | $N_{a,2}$ (/cm$^2$) |
|---|---|---|---|---|---|---|---|---|---|
| 8(a) | $WSe_2$ (2L) [5] | 0.8 | $4.6 \times 10^{12}$ | 0.2 | $3.87 \times 10^{12}$ | 0.9 | $4.09 \times 10^{12}$ | … | … |
| 8(b) | $WS_2$ (bulk) [4] | 0.16 | $3.11 \times 10^{12}$ | … | … | 0.41 | $1.76 \times 10^{12}$ | 0.22 | $1.24 \times 10^{12}$ |
| 8(d) | $MoS_2$(1L) [53] | 0.075 | $9.3 \times 10^{11}$ | 0.1 | $1.1 \times 10^{12}$ | … | … | … | … |
| 8(e) | $WSe_2$ (2L) [2] | 0.2 | $2.7 \times 10^{12}$ | … | … | 0.15 | $2.4 \times 10^{12}$ | 0.28 | $4e \times 10^{11}$ |
| 8(f) | $MoS_2$ (1L) [2] | 0.2 | $3.99 \times 10^{12}$ | 0.4 | $1.8 \times 10^{12}$ | … | … | … | … |

**Note:** The degeneracy factors for donor and acceptor defects ($g_d$ and $g_a$) in 2D semiconductor systems can be obtained from first-principles band structure calculations [51,52]. In our compact modeling, these degeneracy factors $g_{d(a)}$ are generally set to 2 for all the distinct defects.

Refs. [51,52]. And the gate dielectrics are normalized to equivalent dioxide thickness (*EOT*). Other unspecified parameters and the defect profiles are treated as fitting parameters in Fig. 8. The intrinsic parameters employed for device modeling in Fig. 8 are listed in Tables II and III and specify the defect-related parameters. For simplicity, the single-level defects are selected, which causes the undesired knot in the subthreshold region of Fig. 8(b). Figure 8(d) demonstrates the model's ability to describe the same device within an appropriate temperature range [53] without significant fitting parameter readjustment. Our model fitting performance towards oxide gate ($HfO_2$) unipolar 2D FETs [2] is demonstrated in Figs. 8(e) and 8(f). Furthermore, by considering both Ohmic and Schottky contacts [54], the output curves corresponding to Fig. 8(a) are plotted in Sec. S8 of the Supplemental Material [29]. The field-dependent mobility is considered in Sec. S7 of the Supplemental Material [29].

## IV. CONCLUSION

In summary, this work presents a physics-based CPS framework for the compact modeling of 2D FET. By employing the quasiequilibrium approximation and formulating the drain-source current as a path integral within the CPS, the model accurately captures threshold voltage roll-off, saturation current upswing, and ambipolar conduction behavior, etc. Critically, through analyzing the bias-dependent integration path in the CPS, we derive, for the first time, analytical expressions for key electrical turning points across all operating regimes—including threshold voltage $V_{th}$, saturation voltage $V_{\mathrm{sat}}$, pinch-off voltage $V_{\text{pinch-off}}$, and $p$-$n$-junction onset voltage $V_{p\text{-}n\text{-on}}$—with these voltages quantitatively linked to SBH, channel charge, and external electric field. All parameters in the model have clear physical meanings, addressing the drawback of nonphysical numerical fitting in earlier 2D FET compact models.

Furthermore, the model incorporates the effects of ionized defects, overcoming the limitation of previous models that failed to account for degraded subthreshold swing and on-off current ratio. Rigorous validation against experimental data from both ambipolar and unipolar transistors confirms its ability to accurately reflect the devices' excellent electrostatic gating characteristics and uniform thermal dissipation. This study establishes a comprehensive, physics-based 2D FET compact model, laying a more robust foundation for their practical circuit design and manufacturing.

## ACKNOWLEDGMENTS

This work was jointly supported by the Key Research and Development Program of Hunan Province under Grant 2025WK2001, the Natural Science Foundation of China under Grant 62274059, and the "111 Center" (B25033).

## DATA AVAILABILITY

The data that support the findings of this article are openly available [2,4–6,53].

[1] W. Fei, J. Trommer, M. C. Lemme, T. Mikolajick, and A. Heinzig, Emerging reconfigurable electronic devices based on two-dimensional materials: A review, InfoMat **4**, e12355 (2022).

[2] S. Ghosh, Y. Zheng, M. Rafiq, H. Ravichandran, Y. Sun, C. Chen, M. Goswami, Najam U Sakib, Muhtasim Ul Karim Sadaf, Andrew Pannone, Samriddha Ray, Joan M. Redwing, Yang Yang, Shubham Sahay, and Saptarshi Das, A complementary two-dimensional material-based one instruction set computer, Nature **642**, 327 (2025).

[3] W. Hu, Z. Sheng, X. Hou, H. Chen, Z. Zhang, D. W. Zhang, and P. Zhou, Ambipolar 2D semiconductors and emerging device applications, Small Methods **5**, 2000837 (2021).

[4] G. Lee, S. Oh, J. Kim, and J. Kim, Ambipolar charge transport in two-dimensional $WS_2$ metal–insulator–semiconductor and metal–insulator–semiconductor field-effect transistors, ACS Appl. Mater. Interfaces **12**, 23127 (2020).

[5] A. Prakash and J. Appenzeller, Bandgap extraction and device analysis of ionic liquid gated $WSe_2$ Schottky barrier transistors, ACS Nano **11**, 1626 (2017).

[6] Y. J. Zhang, J. T. Ye, Y. Yomogida, T. Takenobu, and Y. Iwasa, Formation of a stable $p$–$n$ junction in a liquid-gated $MoS_2$ ambipolar transistor, Nano Lett. **13**, 3023 (2013).

[7] G. V. Resta, Y. Balaji, D. Lin, I. P. Radu, F. Catthoor, P.-E. Gaillardon, and G. De Micheli, Doping-free complementary logic gates enabled by two-dimensional polarity-controllable transistors, ACS Nano **12**, 7039 (2018).

[8] D. Yeom, Yeonghyeon Ko, Youngkyu Ko, H. Im, Jungi Song, Yongwook Seok, Hanbyeol Jang, Jaeha Hwang, Seokhun Jin, Kenji Watanabe, Takashi Taniguchi, and Kayoung Lee, Ternary transistors with reconfigurable polarities, Adv. Funct. Mater. **35**, 2502112 (2025).

[9] J. Chen, P. Li, J. Zhu, X.-M. Wu, R. Liu, J. Wan, and T.-L. Ren, Reconfigurable $MoTe_2$ field-effect transistors and its application in compact CMOS circuits, IEEE Trans. Electron Devices **68**, 4748 (2021).

[10] D. K. Polyushkin, S. Wachter, L. Mennel, M. Paur, M. Paliy, G. Iannaccone, G. Fiori, D. Neumaier, B. Canto, and T. Mueller, Analogue two-dimensional semiconductor electronics, Nat. Electron. **3**, 486 (2020).

[11] I. S. Esqueda, H. Tian, X. Yan, and H. Wang, Transport properties and device prospects of ultrathin black phosphorus on hexagonal boron nitride, IEEE Trans. Electron Devices **64**, 5163 (2017).

[12] A. V. Penumatcha, R. B. Salazar, and J. Appenzeller, Analysing black phosphorus transistors using an analytic Schottky barrier MOSFET model, Nat. Commun. **6**, 8948 (2015).

[13] N. Haratipour, S. Namgung, S.-H. Oh, and S. J. Koester, Fundamental limits on the subthreshold slope in Schottky source/drain black phosphorus field-effect transistors, ACS Nano **10**, 3791 (2016).

[14] A. Tunga, Z. Zhao, A. Shukla, W. Zhu, and S. Rakheja, Physics-based modeling and validation of 2-D

Schottky barrier field-effect transistors, IEEE Trans. Electron Devices **70**, 2034 (2023).

[15] C. Roemer, Ghader Darbandy, M. Schwarz, Jens Trommer, Andre Heinzig, T. Mikolajick, Walter M. Weber, B. Iñíguez, and A. Kloes, Physics-based DC compact modeling of Schottky barrier and reconfigurable field-effect transistors, J. Electron Device Soc. **10**, 416 (2022).

[16] E. Yarmoghaddam, N. Haratipour, S. J. Koester, and S. Rakheja, a physics-based compact model for ultrathin black phosphorus FETs—Part I: Effect of contacts, temperature, ambipolarity, and traps, IEEE Trans. Electron Devices **67**, 389 (2020).

[17] S. A. Ahsan, S. K. Singh, M. A. Mir, M. Perucchini, D. K. Polyushkin, T. Mueller, G. Fiori, and E. G. Marin, A SPICE compact model for ambipolar 2-D-material FETs aiming at circuit design, IEEE Trans. Electron Devices **68**, 3096 (2021).

[18] L. Deng, J. Li, Q. Liu, H. Huang, J. Wang, D. Cheng, H. Wen, and S. Im, Compact I-V model for ambipolar field-effect transistors with 2D transition metal dichalcogenide as semiconductor, IEEE Trans. Nanotechnol. **19**, 841 (2020).

[19] L. Wang, Y. Li, X. Feng, K.-W. Ang, X. Gong, A. Thean, and G. Liang, in *2017 IEEE International Electron Devices Meeting (IEDM)* (IEEE, San Francisco, CA, USA, 2017), pp. 31.4.1–31.4.4.

[20] Z.-Y. Yan, K.-H. Xue, Z. Hou, Y. Shen, H. Tian, Y. Yang, and T.-L. Ren, Quasi-Fermi-level phase space and its applications in ambipolar two-dimensional field-effect transistors, Phys. Rev. Appl. **17**, 054027 (2022).

[21] C. Guo, L. Wang, H. Xing, and X. Chen, The study of ambipolar behavior in phosphorene field-effect transistors, J. Appl. Phys. **120**, 215701 (2016).

[22] Z. Yan, G.-Y. Gou, J. Ren, F. Wu, Y. Shen, H. Tian, Y. Yang, and T. Ren, Ambipolar transport compact models for two-dimensional materials based field-effect transistors, Tsinghua Sci. Technol. **26**, 574 (2021).

[23] Y. Liu, P. Wang, Y. Wang, Y. Huang, and X. Duan, Suppressed threshold voltage roll-off and ambipolar transport in multilayer transition metal dichalcogenide feed-back gate transistors, Nano Res. **13**, 1943 (2020).

[24] Joseph R. Nasr, Daniel S. Schulman, Amritanand Sebastian, Mark W. Horn, Joshua A. Robinson, and Saptarshi Das, Mobility deception in nanoscale transistors: An untold contact story, Adv. Mater. **31**, 1806020 (2019).

[25] C. Liu, G. Li, R. Di Pietro, J. Huang, Y.-Y. Noh, X. Liu, and T. Minari, Device physics of contact issues for the overestimation and underestimation of carrier mobility in field-effect transistors, Phys. Rev. Appl. **8**, 034020 (2017).

[26] B. Radisavljevic and A. Kis, Mobility engineering and a metal–insulator transition in monolayer $MoS_2$, Nat. Mater. **12**, 815 (2013).

[27] Y. Wang, Jun Xiao, Hanyu Zhu, Yao Li, Yousif Alsaid, King Yan Fong, Yao Zhou, Siqi Wang, Wu Shi, Yuan Wang, Alex Zettl, Evan J. Reed, and Xiang Zhang, Structural phase transition in monolayer $MoTe_2$ driven by electrostatic doping, Nature **550**, 487 (2017).

[28] G.-H. Lee, X. Cui, Y. D. Kim, G. Arefe, X. Zhang, C.-H. Lee, F. Ye, K. Watanabe, T. Taniguchi, P. Kim, and J. Hone, Highly stable, dual-gated $MoS_2$ transistors encapsulated by hexagonal boron nitride with gate-controllable contact, resistance, and threshold voltage, ACS Nano **9**, 7019 (2015).

[29] See Supplemental Material at http://link.aps.org/supplemental/10.1103/dmv5-hsxt for additional information on mathematical details and simulation results, including (1) the relationship between carrier concentration and body and field effects in two-dimensional semiconductors; (2) the generalized Einstein relation in two-dimensional semiconductors; (3) special cases under quasiequilibrium approximation (QEA); (4) the special cases of ESR and MAL under QEA and the origin of Eqs. (13) and (15); (5) the relationship between ionized defect concentrations and field effect & body effect under QEA: (6) output characteristic inflection point considering the influence of defects; (7) the field-dependent mobility correction; (8) the fitting comparison of the output characteristics for the $WSe_2$ ionic liquid gate A2DFET in Fig. 8(a) without and with nonideal contact correction; (9) a specification of the parameters physical meanings and defects related parameter extraction; (10) comparison in currents obtained from full numerical drift-diffusion simulation ($\tau_{tr}$) and quasiequilibrium approximation modeling ($\tau_{qe}$). Above content includes Refs. [55–60].

[30] M. Zhao, Y. Hao, C. Zhang, R. Zhai, B. Liu, W. Liu, C. Wang, S. H. Mujtaba Jafri, A. Razaq, R. Papadakis, J. Liu, X. Ye, X. Zheng, and H. Li, Advances in two-dimensional materials for optoelectronics applications, Crystals **12**, 1087 (2022).

[31] S. M. Sze and K. K. Ng, *Physics of Semiconductor Devices*, 3rd ed. (Wiley-Interscience, Hoboken, NJ, 2007).

[32] V. K. Sangwan and M. C. Hersam, Electronic transport in two-dimensional materials, Annu. Rev. Phys. Chem. **69**, 299 (2018).

[33] D. Vasileska, S. M. Goodnick, and G. Klimeck, *Computational Electronics: Semiclassical and Quantum Device Modeling and Simulation*, 1st ed. (CRC Press, Boca Raton, 2017).

[34] K. P. Ghatak, S. Bhattacharya, and D. De, *Einstein Relation in Compound Semiconductors and Their Nanostructures* (Springer, Berlin, 2009).

[35] E. Yalon, O. J. McClellan, Kirby K. H. Smithe, Miguel Muñoz Rojo, Runjie Lily Xu, Saurabh V. Suryavanshi, Alex J. Gabourie, Christopher M. Neumann, OrcidFeng Xiong, Amir Barati Farimani, and Eric Pop, Energy dissipation in monolayer $MoS_2$ electronics, Nano Lett. **17**, 3429 (2017).

[36] B. Lyu, *et al.*, Graphene nanoribbons grown in hBN stacks for high-performance electronics, Nature **628**, 758 (2024).

[37] D. S. Schulman, A. J. Arnold, and S. Das, Contact engineering for 2D materials and devices, Chem. Soc. Rev. **47**, 3037 (2018).

[38] S. Das, H.-Y. Chen, A. V. Penumatcha, and J. Appenzeller, High performance multilayer $MoS_2$ transistors with scandium contacts, Nano Lett. **13**, 100 (2013).

[39] N. Ali, M. Lee, F. Ali, T. D. Ngo, H. Park, H. Shin, and W. J. Yoo, Percolation-based metal–insulator transition in black phosphorus field effect transistors, ACS Appl. Mater. Interfaces **15**, 13299 (2023).

[40] S. Das, Amritanand Sebastian, Eric Pop, Connor J. McClellan, Aaron D. Franklin, Tibor Grasser, Theresia Knobloch, Yury Illarionov, Ashish V. Penumatcha, Joerg Appenzeller, Zhihong Chen, Wenjuan Zhu, Inge Asselberghs,

Lain-Jong Li, Uygar E. Avci, Navakanta Bhat, Thomas D. Anthopoulos, and Rajendra Singh, Transistors based on two-dimensional materials for future integrated circuits, Nat. Electron. **4**, 786 (2021).

[41] Y. J. Zhang, T. Oka, R. Suzuki, J. T. Ye, and Y. Iwasa, Electrically switchable chiral light-emitting transistor, Science **344**, 725 (2014).

[42] B. W. H. Baugher, H. O. H. Churchill, Y. Yang, and P. Jarillo-Herrero, Optoelectronic devices based on electrically tunable p–n diodes in a monolayer dichalcogenide, Nat. Nanotechnol. **9**, 262 (2014).

[43] L.-R. Zou, D.-D. Sang, Y. Yao, X.-T. Wang, Y.-Y. Zheng, N.-Z. Wang, C. Wang, and Q.-L. Wang, Research progress of optoelectronic devices based on two-dimensional $MoS_2$ materials, Rare Met. **42**, 17 (2023).

[44] H. Zhang, C. Berthod, H. Berger, T. Giamarchi, and A. F. Morpurgo, Band filling and cross quantum capacitance in ion-gated semiconducting transition metal dichalcogenide monolayers, Nano Lett. **19**, 8836 (2019).

[45] J. Cheng, S. Poehler, M. Laskar, L. Ma, S. Kannappan, S. Rajan, Y. Wu, and W. Lu, Temperature dependent carrier transport in few-layered $MoS_2$: from hopping to band transport, J. Phys. Appl. Phys. **55**, 195109 (2022).

[46] W. Dang, Y. Huangfu, M. Hossain, X. Lin, Z. Lu, Z. Huang, Z. Li, Y. Liu, and X. Duan, Self-heating effect in a $MoS_2$ field-effect transistor and improved heat dissipation by the BN capping layer, ACS Appl. Electron. Mater. **6**, 472 (2024).

[47] S. B. Mitta, M. S. Choi, A. Nipane, F. Ali, C. Kim, J. T. Teherani, J. Hone, and W. J. Yoo, Electrical characterization of 2D materials-based field-effect transistors, 2D Mater. **8**, 012002 (2021).

[48] Y. S. Ang, H. Y. Yang, and L. K. Ang, Universal scaling laws in Schottky heterostructures based on two-dimensional materials, Phys. Rev. Lett. **121**, 056802 (2018).

[49] J. S. Ross, S. Wu, H. Yu, Nirmal J. Ghimire, Aaron M. Jones, G. Aivazian, J. Yan, David G. Mandrus, D. Xiao, W. Yao, and X. Xu, Electrical control of neutral and charged excitons in a monolayer semiconductor, Nat. Commun. **4**, 1474 (2013).

[50] D. K. Schroder, *Semiconductor Material and Device Characterization*, 1st ed. (Wiley, New York, 2005).

[51] T. Cheiwchanchamnangij and W. R. L. Lambrecht, Quasiparticle band structure calculation of monolayer, bilayer, and bulk $MoS_2$, Phys. Rev. B **85**, 205302 (2012).

[52] D. Wickramaratne, F. Zahid, and R. K. Lake, Electronic and thermoelectric properties of few-layer transition metal dichalcogenides, J. Chem. Phys. **140**, 124710 (2014).

[53] N. Fang, S. Toyoda, T. Taniguchi, K. Watanabe, and K. Nagashio, Full energy spectra of interface state densities for $n$ - and $p$ -type $MoS_2$ field-effect transistors, Adv. Funct. Mater. **29**, 1904465 (2019).

[54] Z. Yan, Z. Hou, Kan-Hao Xue, H. Tian, T. Lu, J. Xue, F. Wu, R. Zhao, M. Shao, J. Yan, A. Yan, Z. Wang, P. Shen, M. Zhao, X. Miao, Z. Lin, H. Liu, Yi Yang, and Tian-Ling Ren, Landauer-QFLPS model for mixed Schottky-Ohmic contact two-dimensional transistors, Adv. Sci. **10**, 2303734 (2023).

[55] S. V. Suryavanshi and E. Pop, S2DS: Physics-based compact model for circuit simulation of two-dimensional semiconductor devices including non-idealities, J. Appl. Phys. **120**, 224503 (2016).

[56] Y. Zhao, Y. Cai, L. Zhang, B. Li, G. Zhang, and J. T. L. Thong, Thermal transport in 2D semiconductors—considerations for device applications, Adv. Funct. Mater. **30**, 1903929 (2020).

[57] A. Sood, F. Xiong, S. Chen, R. Cheaito, F. Lian, M. Asheghi, Y. Cui, D. Donadio, K. E. Goodson, and E. Pop, Quasi-ballistic thermal transport across $MoS_2$ thin films, Nano Lett. **19**, 2434 (2019).

[58] F. Wu, T. J. Smart, J. Xu, and Y. Ping, Carrier recombination mechanism at defects in wide band gap two-dimensional materials from first principles, Phys. Rev. B **100**, 081407 (2019).

[59] M.-H. Bae, S. Islam, V. E. Dorgan, and E. Pop, Scaling of high-field transport and localized heating in graphene transistors, ACS Nano **5**, 7936 (2011).

[60] S. Islam, Z. Li, V. E. Dorgan, M.-H. Bae, and E. Pop, Role of Joule heating on current saturation and transient behavior of graphene transistors, IEEE Electron Device Lett. **34**, 166 (2013).